Title: Developmental co-emergence of cardiac and gut tissues modeled by human iPSC-derived organoids

Authors: A.C. Silva[1], O.B. Matthys[1,2], D.A. Joy[1,2], M.A. Kauss[1,3], V. Natarajan[1], M.H. Lai[1], D. Turaga[1], A.P. Blair[1], M. Alexanian[1], B.G. Bruneau[1,4,5,6], T.C. McDevitt[1,7,*]

Affiliations:

[1]Gladstone Institutes, San Francisco, CA.

[2]UC Berkeley-UC San Francisco Graduate Program in Bioengineering, San Francisco, CA.

[3]UC San Francisco Graduate Program in Biomedical Sciences, San Francisco, CA.

[4]Roddenberry Center for Stem Cell Biology and Medicine at Gladstone, San Francisco, CA.

[5]Cardiovascular Research Institute, University of California, San Francisco, CA.

[6]Department of Pediatrics, University of California, San Francisco, CA.

[7]Department of Bioengineering and Therapeutic Sciences, University of California, San Francisco, CA.

* Correspondence to: todd.mcdevitt@gladstone.ucsf.edu

Abstract:

During embryogenesis, paracrine signaling between tissues in close proximity contributes to the determination of their respective cell fate(s) and development into functional organs. Organoids are *in vitro* models that mimic organ formation and cellular heterogeneity, but lack the paracrine input of surrounding tissues. Here, we describe a human multilineage iPSC-derived organoid that recapitulates cooperative cardiac and gut development and displays extensive cellular and structural complexity of both tissues. We demonstrate that the presence of endoderm tissue (gut/intestine) in multilineage organoids contributed to the development of the cardiac tissue, specifically cardiomyocyte expansion, compartmentalization, enrichment of atrial/nodal cells, myocardial compaction and functional fetal-like maturation. Overall, this study demonstrates the ability to generate specific cooperative tissues originating from different germ lineages within a single organoid model, an advance that will further the examination of multi-tissue interactions during development and disease.

Keywords:

Organoids, pluripotent stem cells, morphogenesis, co-emergence, cooperative development, endoderm, heart, intestine, atrial/nodal cardiomyocytes

36 **Introduction**

37 The formation of organs during embryogenesis results from a coordinated sequence of
38 morphogenic events that regulate the co-emergence and self-organization of distinct cell
39 populations (Zhang and Hiiragi, 2018). Organoids derived from stem and progenitor cells
40 provide an experimentally tractable model of tissue morphogenesis *in vitro* due to the fact that
41 they differentiate into multiple cell types in a spatially-organized manner and recapitulate
42 functional properties of developing native tissues (Lancaster and Knoblich, 2014;Matthys *et al.*,
43 2020). However, most organoids to date give rise to single tissues in isolation, and lack the
44 mechanical cues and paracrine signaling contributed by neighboring organs that synergistically
45 benefit the trajectory of tissue development *in vivo* (Varner and Taber, 2012;Jung *et al.*,
46 1999;Ishii *et al.*, 2007). Previous attempts to generate multi-tissue organoids in a controllable
47 fashion have mainly involved the fusion of pre-differentiated single-lineage organoids (Koike *et*
48 *al.*, 2019;Bagley *et al.*, 2017).

49 Mesoderm and endoderm display reciprocal interactions during embryonic development
50 that are fundamental to the successful formation of several organs, including the heart (Lough
51 and Sugi, 2000;Schultheiss *et al.*, 1995;Sugi and Lough, 1994). *In vitro* co-culture systems of
52 embryonic germ layer explants and pluripotent stem cells demonstrate that endoderm cells secret
53 cardiac-inductive factors (e.g. Activin A, FGF2) that promote cardiomyocyte formation
54 (Anderson *et al.*, 2016;Rudy-Reil and Lough, 2004;Brown *et al.*, 2010;Uosaki *et al.*, 2012;Sugi
55 and Lough, 1995). However, it has been challenging to determine the effect and sequence of
56 direct interactions between endoderm and mesoderm *in vivo* because interrogation at each stage
57 of development disrupts the natural course of morphogenesis.

58 Here, we generated 3D spheroids of early committed mesendoderm progenitors in a
59 culture medium permissive of multi-lineage differentiation. We observed the co-emergence of
60 mesoderm and endoderm cell lineages, resulting in unique multilineage organoids able to
61 spontaneously organize the formation of complex structures similar to the developing heart and
62 gut. Multiple *in vitro* models have been developed to study various aspects of the heart,
63 including patterning constructs (Ma *et al.*, 2015), gastruloids/organoids (Lee *et al.*, 2020;Rossi *et*
64 *al.*, 2020),(Drakhlis *et al.*, 2021) (development), and engineered microtissues (homeostasis and
65 maturation) (Ronaldson-Bouchard *et al.*, 2018;Hookway *et al.*, 2019;Mills *et al.*, 2017;Macqueen
66 *et al.*, 2018). However, models that recapitulate heart morphogenic dynamics (i.e. gastruloid/
67 organoids) have been mostly obtained with mouse stem cells (Rossi *et al.*, 2020;Lee *et al.*, 2020),
68 and only recently using human induced pluripotent stem cells (iPSCs)(Drakhlis *et al.*, 2021). On
69 the other hand, intestinal tissue has been generated *in vitro* with high reproducibility using mouse
70 and human stem cells derived from tissue biopsies and iPSC (Sato *et al.*, 2009;Munera *et al.*,
71 2017). The cardiac and gut (multilineage) organoid presented here constitutes a first step toward
72 a new generation of organoids that recapitulate the co-development and differentiation of two
73 defined tissues for long periods of time (>1 year). Such defined multi-lineage/multi-organ
74 organoids hold the unique promise of modeling the crosstalk between specific tissues that occurs
75 during human embryogenesis, tissue maturation and disease— a complex phenomenon that is
76 difficult to dissect *in vivo*.
77

78 **Results**

79 **Formation of heart-like compartments in multilineage spheroids**

80 We began by generating spheroids from mesendoderm progenitors differentiated for 5
81 days with the GiWi protocol (Lian *et al.*, 2012). Spheroids were then cultured in conventional,
82 cardiac-permissive medium supplemented with insulin (RPMI/B27+), or in an ascorbic acid
83 (AA)-supplemented medium formulated for epicardial cell differentiation to mimic the signaling
84 that occurs during cardiac differentiation to support the emergence of a variety of cell types (i.e.
85 fibroblasts and smooth muscle cells (SMC))(Bao *et al.*, 2016;Lian *et al.*, 2013) **(Figure 1A,B)**.
86 Noticeable differences in size and structural arrangement between spheroids grown in
87 conventional versus AA medium (hereafter referred to as "conventional" and "multilineage"
88 microtissues, respectively) became evident within 2 weeks of differentiation, with multilineage
89 microtissues growing to approximately 3 times the size of conventional microtissues by 30 days
90 **(Figure 1C, D, E)**. After 10 days, conventional microtissues displayed a spherical, uniformly
91 translucent morphology with spontaneous contractility throughout **(Figure 1C, D; Movie S1)**,
92 whereas the multilineage microtissues exhibited a dark core of vigorously contracting cells
93 surrounded by translucent non-contracting cells. Calcium transients were limited to the central
94 region of contracting cells in the multilineage tissues **(Figure 1C,D; Movie S2)**. At early stages
95 of culture, light-sheet fluorescence microscopy revealed that conventional microtissues were
96 largely composed of cardiomyocytes, as identified by cardiac troponin (cTnT) immunostaining,
97 that co-expressed TBX18 (cTnT+/TBX18+ cells), and an outer layer of TBX18+ epicardial cells
98 (cTnT-/TBX18+) **(Figure 1F; S1A, S2A)**. However, by day 40, conventional microtissues had
99 only small patches of epicardial cells at the surface **(Figure 1F; S2A)**. In contrast, multilineage
100 microtissues displayed a core of cTnT+ cardiomyocytes surrounded by a non-myocyte, stromal-

101 like cell population (phalloidin+, cTnT-), and an outer layer of TBX18+ epicardial cells (cTnT-
102 /TBX18+), which was preserved for more than two month **(Figure 1F; S1A, S2A)**, and better
103 resembled the radial organization of the embryonic heart wall **(Figure S1A)**.
104 Additional histological analysis revealed that both conventional and multilineage microtissues
105 contained SMCs (SMA+/MYH7-; **Figure S2B**). However, in multilineage microtissues,
106 cardiomyocytes positive for the ventricular marker MLC2v aggregated together in the cardiac
107 tissue core, indicating spatial compartmentalization reminiscent of the distinct emergence of
108 atrial and ventricular cardiomyocytes in the primitive heart **(Figure 1G)**; distinct spatial
109 compartmentalization of cardiomyocytes was not observed in conventional microtissues.
110 The dramatic growth of multilineage microtissues over the first 30 days in culture was
111 paralleled by an increase in the volume of the cardiac region **(Figure 1H; S1C, S2C; Movie S3-**
112 **4)**. Cardiac growth appeared to result from cardiomyocyte proliferation, based upon
113 immunostaining for Ki67, a marker of active cell cycle—analogous to cardiac wall thickening
114 during development **(Figure 1H; S1C)**. In addition, at day 30, we observed the emergence of
115 small epithelial cystic structures within the previously translucent layers of cells enclosing the
116 cardiac core in multilineage microtissues **(Figure 1C)**. These cystic structures expressed the
117 mid-hindgut (MHG) endoderm markers FOXA2 and CDX2 **(Figure 1C,I; S2D,E)**. Since the
118 multilineage microtissues contained endoderm epithelial clusters, attained greater structural
119 complexity typical of the cardiac compartment and exhibited growth dynamics comparable to the
120 embryonic heart, they were hereafter referred to as multilineage organoids **(Figure 1J)**
121 (Lancaster and Knoblich, 2014).
122

123 **Long-term culture of multilineage organoids recapitulates embryonic heart and gut**
124 **development**

125 We next examined whether multilineage organoids acquired further complexity with
126 extended time in culture. The growth of multilineage organoids accelerated throughout culture
127 duration, with the average organoid reaching ~2mm in diameter after 100 days **(Figure 2A-C)**.
128 After 50 days, the stromal cells surrounding the cardiac core were replaced by a mesenchymal
129 tissue **(Figure 2D)** enriched in extracellular matrix (ECM) components, such as hyaluronic acid
130 **(Figure S2F),** and a fine fibrillar network of glycosaminoglycans **(Figure 2D, light green/blue)**
131 that was populated by a few *WT1*-expressing cells **(Figure S1A)**. The mesenchymal tissue
132 resembled the interstitial tissue underlying the epicardium (or sub-epicardium) and the
133 peritoneum (protective layer of the intestine) **(Figure 2D)**. In addition, smooth muscle actin
134 (SMA)-positive cells were detected at the surface of the organoid and in the sub-epicardium, and
135 a few endothelial cells (PECAM-1+) appeared interspersed among the cardiomyocytes **(Figure**
136 **2F)**. By day 60, SMCs (αSMA+ MYH7-) emerged prominently between the cardiac and the
137 primitive gut-like tissue. The SMC tissue displayed slow and infrequent calcium transients (~5s
138 duration per transient; 1-3 transients/minute) that corresponded to large contractions (>100 μm)
139 that resembled peristalsis **(Figure 2G,H; Movie S5-6)**. More endothelial cells were detected
140 between the cardiomyocytes, forming branched-like structures resembling pre-vascular networks
141 **(Figure 2F)**. Between 70 and 100 days of differentiation, the primitive gut tissues matured, as
142 shown by the development of Paneth cells (antimicrobial peptide-producing cells) and goblet
143 cells (which produce mucins) **(Figure 2D)**. Thus, multilineage organoids undergo a sequence of
144 morphogenic events that recapitulates the development of the human embryonic heart and gut,

145 including the initial emergence of cardiac tissue followed by gut tissue, with interstitial tissue
146 (sub-epicardium/sub-peritoneum-like tissue) separating the two distinct tissues.
147 To assess the cellular heterogeneity of the multilineage organoids, we performed single-
148 cell RNA-sequencing (scRNA-seq) on dissociated organoids after 100 days. Seurat analysis
149 revealed 6 cell clusters corresponding to cardiomyocytes, SMCs, proliferating cells, fibroblasts,
150 gut and enteroendocrine cells **(Figure 3A-C; S3A; Table S1)**. GO term analysis of the
151 enteroendocrine cell cluster yielded hormone transport and secretion **(**expressing CHGA; **Figure**
152 **3B; S3A**), suggesting the development of chemosensing properties in the gut
153 compartment(Gribble and Reimann, 2016). Sub-clustering of the gut cells confirmed the
154 differentiation of specialized intestinal cells, including: 1) enterocyte-like cells (absorptive cells
155 expressing VIL1, ANPEP, MUC13/17); 2) Paneth cells (expressing LYZ); 3) LGR5-expressing
156 intestinal stem cells; and 4) small intestine cells marked by high expression of APOB, CDX2 and
157 VIL1, along with enrichment of genes for glucose and cholesterol transporters (SLC2A2 and
158 NPC1L1, respectively), and digestion (FABP2, SI, SLC5A1) **(Figure 3C,D; S3A,B)**. The
159 presence of these gut cell types was further validated by electron microscopy of 100-day old
160 multilineage organoids through the identification of key structural features of each cell type
161 **(Figure 2I i-v)**. Goblet cells were not detected by scRNA-seq, presumably due to their larger
162 size.
163 Analysis of cell populations within the cluster enriched for proliferative markers revealed
164 the presence of proliferating cardiomyocytes (TTN, MYH6, NPPA) and SMCs (ACTG2,
165 MYH11) **(Figure S3C,D)**. Ki67 immunostaining demonstrated a decline in the number of
166 actively cycling cells over time **(Figure 2J)**; nevertheless, some cardiomyocytes (slow/fast
167 TnI+), SMCs, and gut cells remained Ki67+ after 100 days in culture, corroborating the scRNA-

168 seq results **(Figure S3G)**. Sub-clustering analysis of the cardiomyocytes indicated that after 100
169 days in culture, cardiomyocytes were divided into 3 groups, separated mainly by differences in
170 maturation stage markers: immature cells that either expressed ECM related genes(Cui *et al.*,
171 2019) (Cluster 2) or smooth muscle myosin (MYH11, Cluster 0), and more mature-like
172 cardiomyocytes (Cluster 1) that expressed higher levels of TNNI3 **(Figure 3E,F)**. A minority of
173 cardiomyocytes (~30%) expressed the ventricular cardiomyocyte markers IRX4 or MYH7
174 **(Figure 3G; 3SA)**, indicating that multilineage organoids favor the differentiation and
175 maturation of atrial cardiomyocytes, as confirmed by the high expression of atrial markers such
176 as TBX5, MYH6 and GJA5 **(Figure 3G)**. Although key atrial and ventricular genes were
177 expressed in the same cluster of cells (Cluster 1), these genes were not co-expressed in individual
178 cells **(Figure S3F)**.
179 To identify *in vivo* correlates, we used a cell type classifier, trained on scRNA-seq of
180 human fetal heart tissue collected at 6.5-7 weeks **(Figure S3H)**(Asp *et al.*, 2019), to characterize a
181 subset of cardiomyocyte, fibroblast and SMC clusters that were identified by default Seurat
182 clustering and cardiac cell compartmentalization genes. The classifier estimated that 98% of the
183 organoid cardiomyocytes were atrial cardiomyocytes (prediction probability = 0.91) **(Figure 3H,**
184 **I; S3G)**, with classification driven by MYH6 expression, a classifier top feature for atrial cell
185 predictions **(Table S2)**. Ventricular cells only represented 1% of the cardiomyocytes (prediction
186 probability = 0.69) **(Figure 3H, I; S3G)**. The cell classifier also identified fibroblast and
187 SMC/Fibroblast-like cells, as expected, which represented 44% and 11% of the cells analyzed
188 with prediction probabilities of 0.85 and 0.75, respectively **(Figure 3H,I)**. In addition, the *in vivo*
189 cell classifier assigned cell type identities not detected using default Seurat clustering analysis,
190 such as sub-epicardial and capillary endothelium/pericytes/adventia cells, which together

191 constituted less than 4% of the total cells evaluated **(Figure 3H,I; S3G)**. Although the capillary
192 endothelium/pericytes/adventia cells corresponded to only 0.1% of the cells, their assignment
193 had a high prediction probability of 1.00 **(Figure 3H; S3G)**. In summary, the *in vivo* cell
194 classifier corroborated the cellular complexity of the multilineage organoids first observed by
195 histological analysis, and suggested a high transcriptomic similarity between cells from
196 multilineage organoids and cells from fetal human hearts **(Figure 3I)**.

197 Multilineage organoids remained viable for over 1 year in culture, and stably maintained
198 their millimeter size-scale and structural complexity **(Figure S4)**. Contractile behavior was
199 observed only when electrical stimulation was applied, a feature consistent with functionally
200 mature iPSC-derived cardiomyocytes (Yang *et al.*, 2014) **(Figure S4B)**. The cardiac and
201 intestine tissues remained localized at opposite ends of the organoids, separated by stromal cells
202 and SMCs **(Figure S4C-E,G)**. In contrast to previous timepoints, small clusters of SMCs were
203 detected amongst the cardiomyocytes in these aged organoids, and SMCs were more pronounced
204 at the boundary of cardiac tissue regions **(Figure S4F)**. In addition, proliferating non-myocytes
205 (Ki67+, cTnT-) were detected within the cardiac tissue, along with structures that resembled
206 mature blood vessels (expressing lectin, a glycoprotein of the basal lamina of endothelial cells)
207 embedded within or adjacent to the cardiac regions in some organoids **(Figure S4C, G)**.
208 Organoids cultured for 1 year proved challenging to dissociate to single cells, potentially due to
209 the structural complexity and ECM composition, thus limiting our ability to capture the
210 morphological features and the transcriptional signature of individual cells.

211 Overall, these observations demonstrate that multilineage organoids represent a new type
212 of compartmentalized organoid model that exhibits the co-development and maturation of tissues

213 derived from two distinct germ layers, heart (mesoderm) and gut (endoderm)(Koike *et al.*,
214 2019;Faustino Martins *et al.*, 2020;Bagley *et al.*, 2017).
215
216 **Multilineage organoids promote atrial/nodal cardiomyocyte specification and maturation**
217 To further assess the maturity and sub-type specification of the cardiomyocytes, we
218 performed electrophysiological and structural analysis of the intact spheroids and dissociated
219 cells. Over time, 100% of conventional microtissues exhibited spontaneous contractility, and
220 33±21% of day-80 conventional microtissues could be paced at 2Hz **(Figure 4A; S5A,B)**.
221 Furthermore, conventional microtissues exhibited no dramatic changes over time in kinetic
222 calcium handling properties (amplitude and stroke velocities) under 1-Hz of stimulation,
223 reflecting relatively immature function **(Figure 4B,C)**. In contrast, multilineage organoids
224 demonstrated a decrease in spontaneous calcium activity over time, from 100% at day 10 to
225 37±16% at day 100, and an ability to respond to higher frequencies of electrical stimulation, up
226 to 8Hz after 80 days of culture **(Figure 4A-D; S5A)**. In addition, after 30 days, multilineage
227 organoids demonstrated progressively increasing amplitude and maximum stroke velocities
228 under 1-Hz of stimulation, consistent with greater functional maturation than the conventional
229 microtissues **(Figure 4B,C).**
230 Morphological analysis of dissociated tissues revealed greater structural maturation of
231 individual cardiomyocytes from day-30 multilineage organoids than conventional microtissues,
232 as determined by greater surface area and perimeter, elongated morphology, and highly-aligned
233 and defined sarcomeres **(Figure 4E-G)**(Lundy *et al.*, 2013). More elongated cardiomyocytes
234 with highly-aligned and defined sarcomeres were isolated from day-80 multilineage organoids,
235 reflecting additional structural maturation over time **(Figure 4F,G)**. Electron microscopic

236 imaging of cardiomyocytes from day-100 multilineage organoids revealed a series of
237 ultrastructural features typical of the third-trimester human fetal heart, including: 1) myofibrils
238 closely packed with defined striations and no apparent M bands **(Figure 4H,i)**; 2) cylindrical-
239 shaped mitochondria aligned between the myofibrils **(Figure 4H,ii)**; and 3) large pools of
240 glycogen vesicles, the major energy source during fetal heart development **(Figure 4H,iii)** (Kim
241 *et al.*, 1992;Racca *et al.*, 2016). This advanced degree of iPSC-derived cardiomyocyte structural
242 features is not commonly observed without external stimuli (mechanical, electrical or chemical),
243 thus highlighting the intrinsic ability of the multilineage organoid model to promote cellular
244 maturation of cardiac muscle cells.

245 We next evaluated cardiomyocyte function using patch-clamp analysis of dissociated
246 single cells, considering multiple action potential parameters (APD_{90}/APD_{50} ratio, APD_{30-}
247 $_{40}/APD_{70-80}$ ratio, MDP, peak, amplitude, frequency, and dV/dTMax). Electrophysiology analysis
248 revealed a higher proportion of atrial and nodal-like (atrial/nodal) cardiomyocytes (day 30: 73%)
249 than found in conventional microtissues (day 30: 57%) **(Figure 4 I,J)**. In addition, the number of
250 atrial/nodal cardiomyocytes increased over time (multilineage organoids day 30: 73%, day 60:
251 80%) **(Figure 4 I,J)**, consistent with the assignment of 98% of cardiomyocytes as atrial-like cells
252 by the *in vivo* cell classifier at day 100 **(Figure 3H; S3G)**. These results reflect the ability of
253 multilineage organoids to specify and mature atrial/nodal cardiomyocytes, which has been
254 challenging to achieve by alternative 3D differentiation methods.

255 The primary differences between the multilineage and conventional media are the
256 concentrations of ascorbic acid (AA) and calcium. Previous studies have demonstrated that these
257 two components can influence cardiomyocyte differentiation and maturation, respectively(Cao *et*
258 *al.*, 2012;Wheelwright *et al.*, 2018). To assess the potential impact of different culture medium

259 components alone on cardiomyocyte specification and maturation, patch-clamp analyses were
260 performed in iPSC-cardiomyocytes differentiated in monolayers in conventional cardiac media
261 (Ca^{2+}= 0.42mM), multilineage media (AA=100µg/ml, Ca^{2+}=1.05mM) and conventional cardiac
262 media supplemented with AA and calcium (AA=100µg/ml, Ca^{2+}=0.63mM). The AA- and Ca^{2+}-
263 supplemented conventional cardiac media enhanced ventricular cardiomyocyte maturation by
264 promoting an increase in peak, amplitude and upstroke velocity (V/s) of the action potentials, but
265 did not promote the emergence of atrial/nodal cardiomyocyte subtypes (no atrial/nodal cells were
266 identified) **(Figure S5C-E)**. Cardiomyocytes differentiated in multilineage medium (in 2D
267 monolayers) exhibited comparable maturation to those in the supplemented conventional media,
268 but yielded mainly ventricular-like cells (97%) **(Figure S5C-E)**. Therefore, although the media
269 components promoted functional cardiomyocyte maturation, they alone were not sufficient to
270 direct atrial/nodal specification. Furthermore, these experiments suggest that the co-development
271 of the gut tissue, which is absent in conventional cardiac microtissues and 2D monolayers,
272 appears to be a critical factor responsible for enrichment of atrial/nodal cardiomyocytes (>90% at
273 day 100; **Figure 3H, S3J**) and the physiological maturation of cardiac tissue in multilineage
274 organoids to an equivalent level of third-trimester human fetal hearts.
275

276 **Multilineage organoids express cardiac and gut master regulatory genes**

277 Many iPSC differentiation protocols suffer from inherent variability in consistency
278 (Volpato and Webber, 2020;Matthys *et al.*, 2020). In our system, when multilineage organoids
279 failed to develop, spheroids instead yielded either solely cardiac microtissues or gut organoids
280 **(Figure 5A,B; S6)**. Despite batch-to-batch differences in spheroid phenotype, all spheroids
281 (n>200) within a single batch derived from the same initial differentiation of progenitor cells

282 manifested identical morphologies and cellularity **(Figure 5A)**. Thus, we hypothesized that
283 subtle differences in the cellular composition of the initial 2D populations of differentiating cells
284 were responsible for the phenotypic outcomes of the spheroids.

285 To evaluate the variability between the starting progenitor populations that gave rise to
286 cardiac microtissues, multilineage organoids, or gut organoids, we performed retrospective
287 analysis of the initial progenitor cell population at day 5 of differentiation by bulk RNA-
288 sequencing, immediately prior to spheroid formation **(Figure 5B)**. Multidimensional scaling
289 (MDS) analysis of the progenitor transcriptomes revealed that different batches had distinct gene
290 expression profiles, and that the progenitors of multilineage organoids represented a unique
291 transcriptional state, roughly equidistant from both cardiac and gut progenitors **(Figure 5C)**.
292 Comparative analysis between cardiac microtissue and gut organoid progenitors indicated that
293 cardiac microtissue progenitors displayed a muscle development-restricted gene expression
294 program. In contrast, progenitors of gut organoids revealed activation of a broader embryonic
295 developmental program, including forebrain, heart, visual and sensory system development
296 **(Figure S7B)**. To dissect the specific transcriptomic features enabling multilineage organoid
297 formation, differential expression analysis was performed to compare the multilineage
298 transcriptional profile to gut organoid and cardiac microtissue progenitors independently.
299 Compared to cardiac microtissue progenitors, multilineage organoid progenitors were enriched
300 in genes related to muscle tissue development and function (*MYH6*, *MYOM1*, *TTN*), as well as
301 transcription factors (TFs) expressed by cardiomyocytes (*MEF2C*, *NKX2-5*, *ISL1*) **(Figure 5D)**,
302 suggesting an increased cardiac signature in the multilineage progenitors. Compared to gut
303 organoid progenitors, multilineage progenitors exhibited a gene expression enrichment of the
304 muscle tissue development program (*ACTC1*, *MYH6*, *MYOM1*) **(Figure 5E)**. No gene ontology

305 term enrichment was observed for the gut organoid progenitors relative to the multilineage
306 progenitors, presumably due to the fact that: 1) the population of gut progenitors express markers
307 of early cardiac differentiation similar to the multilineage progenitors, 2) at early time points
308 (before 20 days), gut organoids phenotypically resemble multilineage spheroids, and 3) and gut
309 tissue development required at least 2 months of 3D culture to manifest clearly with pronounced
310 villi only evident after 100 days **(Figure 5A, S6, S7A; Movie S8)**. Histological analysis revealed
311 that primitive gut structures emerged earlier in the gut organoids **(Figure S7A, day 12)**, however
312 similar structures were not seen in multilineage organoids until later time points **(Figure 5A, day**
313 **20-30; Movie S8)**. Thus, the accelerated development of primitive cystic structures in gut
314 organoids might have disrupted the cardiac morphogenesis originally present in multilineage
315 organoids.

316 In order to dissect specific gene expression differences between multilineage and cardiac
317 or gut progenitors, a targeted pairwise analysis was performed for heart patterning transcription
318 factors, cardiac progenitors and endoderm-related genes. Multilineage progenitors expressed
319 higher levels of T-box (TBX) transcription factors (*TBX2, TBX5, TBX18, TBX20*) that regulate
320 the developing heart(Stennard and Harvey, 2005) , in comparison with the gut progenitors,
321 revealing a broader activation of the cardiac patterning program. Notably, in contrast to the
322 cardiac progenitors, multilineage progenitors expressed higher levels of TBX genes related to
323 sinoatrial node formation (*TBX18*) and chamber formation and septation (*TBX5*), in addition to
324 *HEY1,* a gene whose expression is restricted to the atria in the context of the heart(Rutenberg *et*
325 *al.*, 2006), suggesting a transcriptomic profile more consistent with atrial/nodal cardiomyocyte
326 specification. Furthermore, multilineage progenitors expressed several TFs expressed by cardiac
327 cells (*ISL1*, *NKX2-5*, *TBX5*) and epicardial-related genes (*TBX18*, *CDH1, ALDH1A2, SEMA3D*)

328 at higher levels than cardiac progenitors **(Figure 5F, top)**, consistent with the greater cardiac cell
329 diversity observed in the multilineage organoids as compared to the cardiac microtissues **(Figure**
330 **5A)**. Progenitors yielding multilineage organoids also expressed genes involved in gut tube
331 development (*SOX17*, *ONECUT2*), although at lesser levels than gut organoid progenitors
332 (notably for *SOX17*), suggesting that the multilineage populations contained a smaller number or
333 proportion of gut progenitors **(Figure 5F, bottom)**. In total, multilineage organoid progenitors
334 displayed a mixed transcriptomic profile of cardiac and gut progenitors, which could account for
335 their ability to give rise to organoids consisting of both heart and gut cells.
336
337 **Multilineage organoid progenitors express cardiac and gut relevant paracrine factor genes**
338 Distinct endoderm subtypes are known to play a role in cardiomyocyte formation through
339 paracrine signaling mechanisms (Holtzinger *et al.*, 2010;Brown and Badylak, 2014;Anderson *et*
340 *al.*, 2016). To examine potential intercellular paracrine signaling affecting the co-emergent
341 populations, we compared the expression of genes associated with secreted factors between the
342 different progenitor populations **(Figure 5G)**. We first generated a list of secreted factors that
343 were differentially enriched in the cardiac or gut progenitors **(Figure S7D)**. FGF10 and NPPB
344 were identified among the gut-enriched factors. FGF10 is a growth factor that enhances
345 cardiogenic specification, fetal cardiomyocyte proliferation, and has been identified as a second
346 heart field (SHF)-specific marker, indicating a role in heart tissue development (Al Alam *et al.*,
347 2015;Rochais *et al.*, 2014;Kelly *et al.*, 2001;Chan *et al.*, 2010). NPPB is highly expressed during
348 cardiogenesis, particularly in the differentiating chamber myocardium (Sergeeva and
349 Christoffels, 2013). However, FGF10 and NPPB also promote intestinal cell proliferation,
350 induction of goblet cell differentiation and homeostasis of mesenteric and intestinal tissue(Al

351 Alam *et al.*, 2015;Rochais *et al.*, 2014;Kelly *et al.*, 2001;Sergeeva and Christoffels, 2013). Thus,
352 FGF10 and NPPB could enhance aspects of both cardiac and gut tissue formation. Indeed,
353 multilineage progenitors expressed higher levels of FGF10 and NPPB than the cardiac tissue
354 progenitors **(Figure 5G, top; S7E, left)**. Multilineage progenitors also expressed higher levels of
355 cardiac-enriched factors than the gut progenitors, such as the growth factors IGF1 and ANGPT1,
356 and the ECM proteins DCN and LUM **(Figure 5G, bottom; S7E, right)**. IGF1 enhances
357 mesodermal cell differentiation and subsequent cardiac progenitor cell formation (Engels *et al.*,
358 2013), and ANGPT1 supports proper atrium chamber morphogenesis (Kim *et al.*, 2018). DCN
359 and LUM, matrix molecule genes enriched in the multilineage progenitors, contribute to the
360 structure and mechanics of the heart by binding to core matrix proteins like collagen I and III,
361 and facilitate thickening of collagen fibrils, respectively, thereby impacting collagen
362 fibrillogenesis (Chakravarti, 2002;Ferdous *et al.*, 2007). Hence, multilineage progenitors
363 expressed increased levels of secreted factor genes relevant to both cardiac and gut tissue
364 morphogenesis compared to either individual tissue alone.

365 In summary, this retrospective analysis revealed that, in addition to the emergence of
366 cardiac cells within the multilineage organoids, the co-development of gut alongside cardiac
367 cells potentially contributes to more structurally and functionally mature cardiac tissue via the
368 secretion of key cardio-inductive molecules.

369 **Discussion**

370 Although organoids can recapitulate many physiological properties of tissue development
371 *in vitro*, they typically lack the cooperative paracrine interactions between adjacent tissues that
372 characterize embryogenesis, as well as the diverse multilineage progenitors essential for the
373 development of complex organs such as the heart. Current strategies to increase organoid
374 complexity have focused on the fusion of differentiated organoids (Koike *et al.*, 2019;Bagley *et*
375 *al.*, 2017), but these approaches miss the interactions between germ layers that occur during the
376 early steps of embryogenesis to initiate the formation of different organs. Although a couple of
377 recent reports demonstrate the ability to generate primitive cardiac tissues coincident with
378 endoderm derivatives from pluripotent stem cells with greater fidelity than traditional embryoid
379 body differentiation (Rossi *et al.*, 2020;Drakhlis *et al.*, 2021), such organoids consist of many
380 cell types from different germ lineages. However, in contrast, here we describe a multilineage
381 organoid model system in which only cardiac (mesoderm) and gut (endoderm) tissues emerge in
382 a sequential manner. This multilineage organoid recapitulates morphogenic events that lead to
383 the emergence of key structural features of the developing human heart and gut. Past studies of
384 the interactions between heart and gut during development indicated that endoderm-derived cells
385 generate paracrine signals and mechanical forces that support heart formation (Rudy-Reil and
386 Lough, 2004;Brown *et al.*, 2010;Uosaki *et al.*, 2012;Sugi and Lough, 1995;Kidokoro *et al.*,
387 2018)·(Hosseini *et al.*, 2017;Kelly *et al.*, 2001;Drakhlis *et al.*, 2021;Rossi *et al.*, 2020).
388 Consistent with those findings, our multilineage organoid also demonstrates that endoderm-
389 derived cells can positively impact cardiomyocyte phenotype, suggesting a broad contribution of
390 endoderm-derived cells to heart morphogenesis.

391 We generated multilineage organoids by aggregating early committed mesendoderm
392 progenitors derived from human iPSCs in permissive media conditions. The sequential
393 emergence of functional cardiac and gut-like tissues mimicked human embryonic
394 morphogenesis, in which the first heart beat (3 weeks of gestation) is followed one week later by
395 the extension of the gut tube into fore-, mid- and hind-gut structures (Hill, 2020b;Hill, 2020a). At
396 early stages of *in vitro* culture, multilineage organoids resemble human fetal heart formation (~5
397 weeks of gestation), evidenced by the formation of a surface layer of epicardial cells and a core
398 of cardiomyocytes. Similar features were also observed in conventional microtissues, derived
399 from progenitors spheroids cultured in cardiac-permissive medium. However, only multilineage
400 organoids exhibited significant growth and preserved the exterior epicardial layer over the long
401 term, as well as, a preferential differentiation into atrial/nodal cells, in stark contrast to other
402 cardiac organoid models that also contain endoderm-derived cells(Rossi *et al.*, 2020;Drakhlis *et*
403 *al.*, 2021). The epicardium is an important source of IGF2, a potent cardiac mitogen involved in
404 cardiac wall thickening (Shen *et al.*, 2015;Perez-Pomares and De La Pompa, 2011). It also
405 generates cardiac fibroblasts and smooth muscle cells (SMCs) that invade the heart following an
406 epithelial-to-mesenchymal transition (Smits *et al.*, 2018). Similarly, in our organoid model, we
407 observed cardiomyocyte expansion, as well as the later emergence of SMCs and endothelial cells
408 (which occurs at >5 weeks of gestation in human fetal heart)(Smits *et al.*, 2018;Hirakow, 1983).
409 We propose that the co-emergence of multiple key progenitor cells contributed to the cellular and
410 structural complexity of the cardiac compartment of the multilineage organoids.
411 The presence of gut tissue developing alongside the cardiac tissue improved the
412 phenotypic and functional maturation of the organoid cardiomyocytes, whose structural features
413 resembled those of native third-trimester human fetal heart. To date, more mature features of

414 cardiomyocytes have only been achieved *in vitro* by subjecting early contractile iPSC-derived
415 cardiomyocytes on a 3D collagen gel to an increasing regimen of electrical stimulation
416 (Ronaldson-Bouchard *et al.*, 2018). Additionally, the prevailing view of atrial and ventricular
417 cardiomyocyte specification is that the different cardiomyocyte subtypes derive from distinct
418 mesoderm populations (Lee *et al.*, 2017;Devine *et al.*, 2014). Our organoid model shows that the
419 emergence of cardiomyocytes with an atrial/nodal phenotype occurs in parallel with the
420 formation of primitive gut: whereas at day 20, multilineage organoids contained equivalent
421 amounts of ventricular (MLC2V+) and atrial/nodal (MLC2V-) cardiomyocytes, by day 30, when
422 primitive mid-hindgut (MHG) structures emerged, the proportion of atrial/nodal cardiomyocytes
423 was greater **(Figure 2 D,E)**. Therefore, we speculate that similar to other endoderm subtypes
424 MHG endoderm secretes factors that impact the development of the heart, and specifically
425 promotes atrial/nodal specification. Indeed, previous studies have shown that other endoderm
426 derivatives, such as anterior visceral endoderm and anterior foregut, promote cardiac mesoderm
427 specification and formation of new cardiomyocytes through the secretion of cardiac-inductive
428 factors, like Activin A and FGF2 (Sugi and Lough, 1995;Mummery *et al.*, 2003;Anderson *et al.*,
429 2016;Lough and Sugi, 2000). FGF2 is also expressed by the epithelial, stromal, and SMCs in the
430 intestine, but its effects on gut development have not been fully defined (Dignass and Sturm,
431 2001;El-Hariry *et al.*, 1997). Our multilineage organoid model of cardiac and gut co-emergence
432 offers a novel platform to investigate how specific neighboring tissues synergistically interact to
433 promote co-development and functional maturation.

434 The complexity of the intestinal tissue in multilineage organoids mimics that of the small
435 intestinal mucosa that forms adjacent to enteric SMCs. The formation of an SMC layer in close
436 proximity to the gut epithelium in our multilineage organoids is notable since SMCs have so far

437 only been observed in gut organoids after *in vivo* transplantation (Munera *et al.*, 2017).
438 Furthermore, the SMCs in multilineage organoids exhibited spontaneous peristaltic-like
439 contractility, which has only been observed in fully mature cells *in vivo*, or in *in vitro* cultures of
440 primary cells together with stromal cells and gut pacemaker cells (interstitial cells of Cajal)
441 seeded onto a scaffold (Gays *et al.*, 2017;Kobayashi *et al.*, 2018). Other gut organoid models
442 form an intestine-like mucosa only upon embedding in an exogenous extracellular matrix (i.e.
443 Matrigel) (Munera *et al.*, 2017;Sato *et al.*, 2009). Thus, our organoid model creates a
444 microenvironment permissive for gut tissue formation in the absence of exogenous extracellular
445 matrix components or morphogenic signaling cues, likely due, in part, to the enrichment of ECM
446 components (e.g. glycosaminoglycans and hyaluronic acid) detected in the sub-epicardial/
447 peritoneum-like region where the gut epithelium clusters arise.
448 While multilineage organoids arose robustly from all the aggregated spheroids within a
449 single experiment, not all differentiation experiments gave rise to multilineage organoids. In
450 those alternative instances, we obtained gut organoids or cardiac microtissues instead, at similar
451 frequencies, from the same initial aggregation and culture conditions. Gene expression analysis
452 of the starting populations that yielded the different phenotypic outcomes indicated that
453 multilineage organoids result from progenitors with enriched expression of heart-related
454 patterning TFs, cardiomyocyte contractile machinery related genes, and SOX17, a definitive
455 endoderm master regulator gene. By contrast, cardiac microtissue progenitors expressed a
456 transcriptome that was less enriched for heart cell related genes, and gut organoid progenitors
457 strongly expressed the endoderm marker, SOX17. The expression of endoderm-specific genes at
458 the progenitor stage suggests that not all cells undergo the intended cardiac mesoderm
459 commitment, and that the subsequent emergence of intestinal tissue in the multilineage and gut

460 organoids results from the permissive culture medium supporting the expansion and
461 differentiation of the endoderm progenitors. The analysis of genes encoding secreted molecules
462 in the gut organoid progenitors revealed high expression of FGF10, which functions as an
463 autocrine and paracrine signaling molecule in heart development as well as in the gut, where it
464 regulates the balance between goblet and Paneth cells (Al Alam *et al.*, 2015;Rochais *et al.*,
465 2014;Kelly *et al.*, 2001). Our multilineage organoid model can be useful for the future dissection
466 of paracrine interactions between cardiac and gut tissues, and identification of specific factors
467 that promote morphogenesis and maturation of adjacent tissues.

468 Future efforts can also focus on more robustly controlling the proportion of mesoderm
469 and endoderm cells in the initial progenitor pool. By modulating the expression of cardiac and
470 gut regulatory genes in distinct sub-populations of progenitors, it should be possible to reduce
471 batch-to-batch variability when generating multilineage organoids. Genetic engineering
472 approaches have been demonstrated to control cellular patterning and subsequent adoption of
473 divergent cell fates – fundamental first steps to regulate phenotypic co-emergence and
474 morphogenesis of human iPSC-derived organoids(Libby *et al.*, 2019;Libby *et al.*, 2018;Mackay
475 *et al.*, 2014). In addition, we envisage that "mosaic" transcriptional modulation approaches can
476 be expanded for the development of multilineage organoids that support the co-emergence of
477 distinct tissues other than heart and gut.

478 Overall, our model represents a new class of organoids characterized by the co-
479 development and maturation of two distinct tissues arising from a mixed pool of mesendoderm
480 progenitors. This organoid model opens new avenues to study genetic diseases that affect both
481 the heart and the gut that have been challenging to investigate, such as chronic atrial and
482 intestinal dysrhythmias (Chetaille *et al.*, 2014). Organoids have been primarily developed with

483 the intent to model individual tissues in isolation (Munera *et al.*, 2017;Takasato *et al.*, 2016), and
484 to date only limited attempts have been made to generate more complex and heterotypic
485 organoids, mostly via fusion of pre-differentiated cells and/or organoid tissues (Xiang *et al.*,
486 2017;Koike *et al.*, 2019;Bagley *et al.*, 2017). In contrast, multilineage organoids demonstrate that
487 two specific tissues from distinct germ lineages can arise in parallel within a single spheroid to
488 synergistically support each other's development, and thus will be useful to advance the
489 understanding of cell or tissue interactions during early tissue specification, structural and
490 functional maturation, and/or disease development. Although they may not mimic all aspects of
491 human development, multilineage organoids do offer a more direct view into tissue cross-talk
492 mechanisms than alternative *in vitro* systems or animal models currently in use. Multilineage
493 organoids represent a logical next step in the generation of more physiological *in vitro* models of
494 human development, and therefore broaden the possibilities for modeling early embryogenesis or
495 complex multi-organ disorders *ex vivo*.
496

Acknowledgments:
The authors would like to thank the Stem Cell Core (Dr. Po-Lin So), Histology and Light Microscopy Core (Dr. Meredith Calvert) and Genomics Core (Dr. Natasha Carli and Jim McGuire) at Gladstone Institutes, and Electron Microscopy Lab (Dr. Danielle Jorgens) at UC Berkeley for all the help and expertise shared. The authors thank Dr. Bruce Conklin's laboratory for providing WTC11 GCaMP iPS cell line, Dr. Deepak Srivastava's laboratory for providing antibodies against MYL2 and MYL3, and Dr. Katja Schenke-Layland for providing human fetal heart paraffin blocks. A special thanks to Drs. Tracy Hookway, Irfan Kathiriya, Sanjeev Ranade and Elphège Nora for critical discussions of this work. The authors also acknowledge the Gladstone Scientific Editing Department (Drs. Francoise Chanut and Kathryn Claiborn) for assistance with manuscript editing. This work was supported by the California Institute of Regenerative Medicine Grant (LA1_C14-08015) and the Gladstone BioFulcrum Heart Failure Research Program.

Author contributions: A.C.S. and T.C.M. conceived the study, interpreted the data, and wrote the manuscript. A.C.S. performed iPSC differentiations, microtissues formation and maintenance, histology studies, preparation of the cells for patch clamp analysis, calcium imaging, bulk and single-cell RNA-seq experiments and scRNA-seq analysis. O.B.M. acquired and analyzed calcium flux analysis, assisted on microtissues maintenance. M.H.L. performed patch clamp data acquisition and analysis. D.A.J. developed the python script for calcium flux and patch clamp analysis, performed the alignment of single-cell and bulk RNA-seq data and assisted with the single-cell and bulk RNA-seq analysis. M.A.K. and V.N. prepared bulk RNA-seq libraries and assisted in microtissue maintenance. D.T. performed light sheet microscopy and analysis. A.P.B. performed the *in vivo* cell classifier analysis and with B.G.B. contributed to interpretation of the results. M.A. and B.G.B. assisted with bulk RNA-seq data analysis and B.G.B. contributed to experimental design and interpretation of results. O.B.M., D.A.J., M.A.K, V.N., M.A., and B.G.B. contributed to manuscript editing and discussion.

Competing interests: T.C.M. is a consultant for Tenaya Therapeutics. B.G.B. is a co-founder of and owns equity in Tenaya Therapeutics. The other authors declare no competing interests.

528 **Figures:**

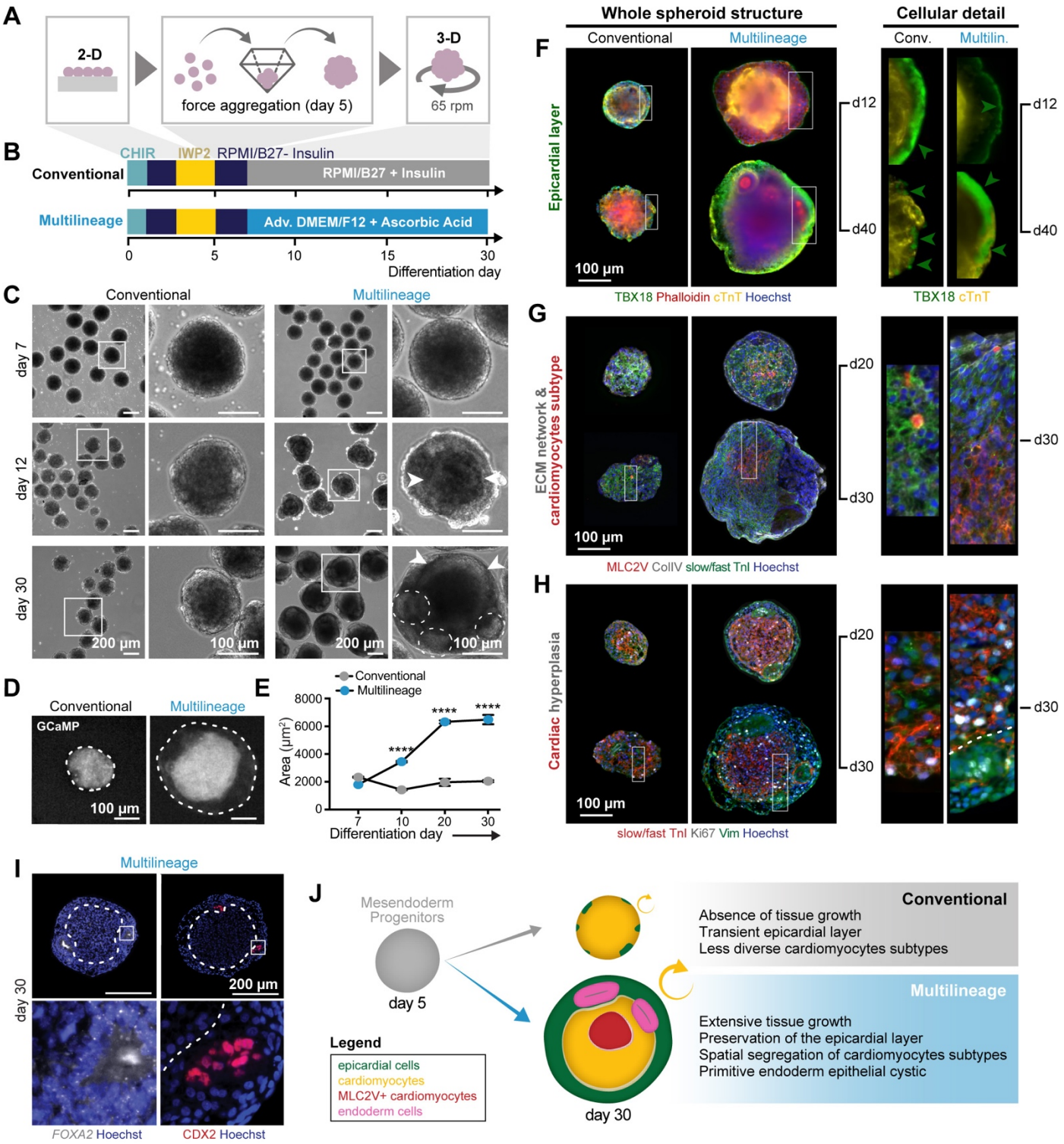

529

530 **Figure 1.** Derivation of a multilineage organoid with complex cardiac structures. **A-B** Overall

531 schematic of conventional and multilineage microtissue formation. **C.** Brightfield images of

532 conventional and multilineage microtissues over the course of 30 days in cell culture; high
533 magnification views of the regions within white squares (right). Multilineage microtissues
534 develop a compact dark core of cells (arrowheads) and epithelial-like structures (dashed outlines)
535 at the surrounding translucent region. **D.** Calcium flux transients visualized by GCAMP are
536 limited to the center area of the multilineage microtissues, whereas they occur throughout the
537 conventional microtissues. Dashed line: microtissue boundaries. **E.** Multilineage microtissues
538 increase in surface area throughout a 30-day culture. Representative experiment. Conventional
539 vs. Multilineage: ****$p<0.0001$. **F-I.** Structural dynamics and cell composition of conventional
540 and multilineage organoids over the course of 30-40 days in culture. **F.** Representative light-
541 sheet imaging of microtissues stained for cardiac Troponin T (cTnT) and TBX18. Conventional
542 microtissues are composed of cardiomyocytes positive for cTnT covered by a continuous outer
543 layer of epicardial-like cells (cTnT-/TBX18+). However, the epicardial coverage shrinks over
544 time to small patches of cells. Multilineage microtissues contain a core of cardiomyocytes
545 (cTnT+/TBX18-) surrounded by stromal-like cells positive for phalloidin and a continuous outer
546 layer of epicardial-like cells (cTnT-/TBX18+). Like in conventional microtissues, the epicardial
547 layer of the multilineage microtissues suffers some disruption throughout the course of the
548 culture, but overall is better preserved over time. Arrowhead: epicardial layer. **G.** Multilineage
549 microtissues evidence a collagen IV network and MYL2+ cardiomyocytes that cluster at the
550 center of the microtissues. Conventional microtissues demonstrate a network of collagen IV at
551 day 20 (d20), but it was not evident at later stages. No MYL2+ positives cells were detected in
552 conventional microtissues. **H.** Multilineage microtissues exhibit more actively cycling (ki67+)
553 cardiomyocytes and non-cardiomyocytes than conventional microtissues. **I.** At day 30,
554 multilineage organoids develop epithelial-like structures positive for mid-hindgut markers
555 (*FOXA2*/CDX2). **J.** Schematic of the main contrasting features between conventional and
556 multilineage microtissues. Due the fact multilineage microtissues contained epithelial endoderm,
557 displayed greater cardiac structural complexity, and exhibited extensive growth dynamics, they
558 were hereafter referred to as multilineage organoids.
559

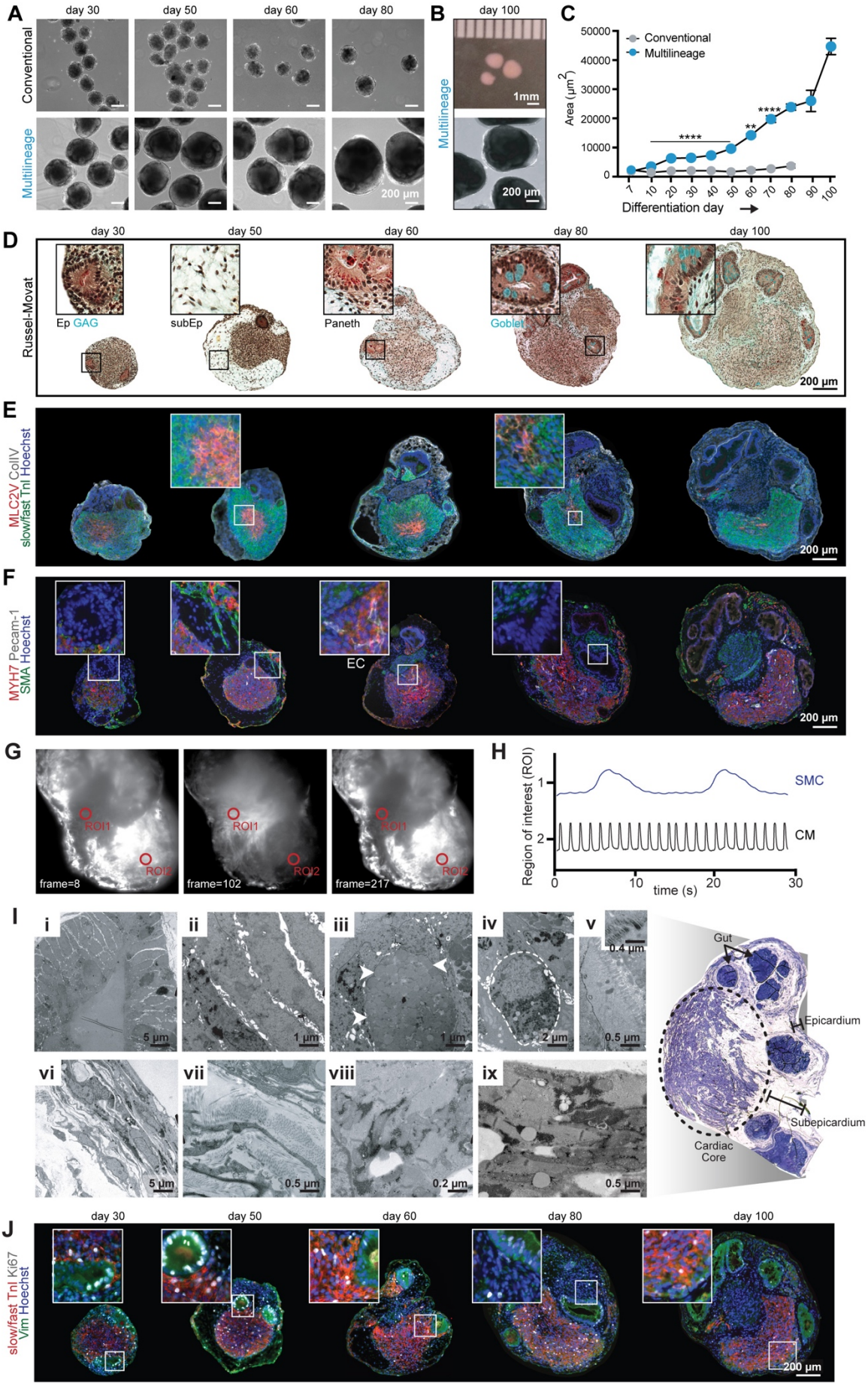
A
day 30
day 50
day 60
day 80
Conventional
Multilineage
200 µm
B
day 100
Multilineage
1mm
200 µm
C
Conventional
Multilineage
Area (µm²)
Differentiation day
D
day 30
day 50
day 60
day 80
day 100
Russel-Movat
Ep GAG
subEp
Paneth
Goblet
200 µm
E
MLC2V CollV
slow/fast TnI Hoechst
200 µm
F
MYH7 Pecam-1
SMA Hoechst
EC
200 µm
G
ROI1
ROI2
frame=8
frame=102
frame=217
H
SMC
CM
Region of interest (ROI)
time (s)
I
i
ii
iii
iv
v
vi
vii
viii
ix
5 µm
1 µm
2 µm
0.5 µm
0.4 µm
0.2 µm
Gut
Epicardium
Subepicardium
Cardiac Core
J
day 30
day 50
day 60
day 80
day 100
slow/fast TnI Ki67
Vim Hoechst
200 µm

560

561 **Figure 2.** Long-term culture of multilineage organoids recapitulates early heart and gut
562 development. **A.** Brightfield microscopy images of conventional and multilineage tissues over
563 days 30 to 80 of culture. Conventional microtissues are viable until day 80 and beyond, whereas
564 conventional microtissues degenerate. **B.** Stereoscope macroscopy (top) and brightfield (bottom)
565 images of day-100 multilineage organoids. **C.** Multilineage organoids display an increase in
566 surface area until day 100 of culture. Representative experiment. Conventional vs. Multilineage:
567 **$p<0.005$, ****$p<0.0001$. **D-F.** Structural dynamics and cell composition of multilineage
568 organoids over the course of the culture as revealed by Russel-Movat stain (D) and fluorescent
569 immunostaining (E-F). **G-H.** Representative images (G) and traces (H) of spontaneous calcium
570 flux transients of the smooth muscle cells (ROI 1) and cardiomyocytes (ROI 2) of a multilineage
571 organoid imaged via light sheet microscopy (Movie S6). **I.** Transmission electron microscopy of
572 the gut structures (i-v), epicardium/subepicardium (vi-vii) and cardiac core (viii-ix). GAG,
573 glycosaminoglycans; Ep, epithelial-like structures; subEp, subepicardium-like tissue; Endo,
574 endothelial cells network; Arrowheads, goblet cell (iii); Dashed line, Paneth cell (iv). **J.** The
575 number of actively cycling cells (Ki67+) decreases over time in multilineage organoids.
576

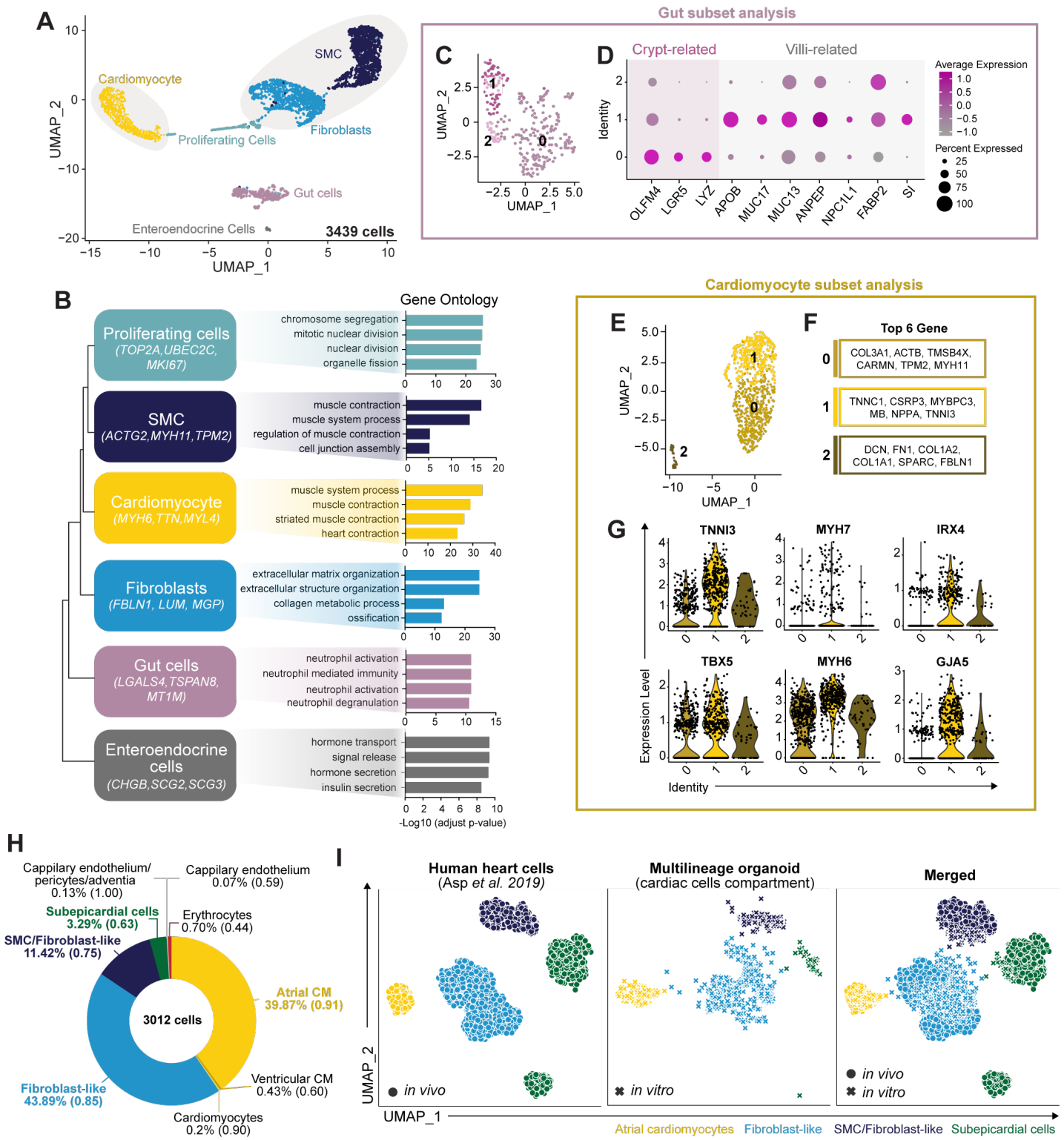

577

578 **Figure 3.** Single-cell transcriptomic analysis at day 100 reveals complex cellular heterogeneity

579 of multilineage organoids. **A.** UMAP plot of all cellular populations identified. Light gray:

580 Seurat cell clusters analyzed using an *in vivo* heart cells classifier. **B.** Cluster tree analysis of the
581 cell clusters with top differentially expressed genes defining each cluster (left) and gene ontology
582 analysis of associated biological processes (right). **C-D.** A sub-clustering analysis of the gut cells
583 evidenced 3 main cell clusters (C) distinguished by the expression of crypt-related or villi-related
584 genes (D): cluster 0 composed mainly of crypt cells (OLFM4), such as gut stem cells (LGR5)
585 and Paneth cells (LYZ); and cluster 1 and 2, constituted by cells at the villi, the enterocytes,
586 identified by the expression of genes related to transmembrane mucins (MUC13, MUC17),
587 digestion (ANPEP, FABP2, SI) and cholesterol transporter genes (NPC1L1), as well as APOB, a
588 gene expressed in the small intestine. **E-F.** Subset analysis of the cardiomyocyte cluster (E) and
589 top-6 genes of the three sub-clusters (F) identify clusters 0 and 2, composed of more immature
590 cardiomyocytes, and cluster 1, composed of more mature cells. **G.** Violin plots of secondary
591 cardiomyocyte analysis depicting expression of key cardiomyocyte subtype genes for
592 ventricular- (top) and atrial-like cells (bottom). **H.** Identity of the cardiac-like cells of
593 multilineage organoids, as determined by a cell classifier trained on expression data from human
594 fetal heart cells. The classifier was applied to the multilineage organoid cardiomyocyte,
595 fibroblast and smooth muscle cells (SMC) clusters identified by Seurat analysis. Data displayed
596 include cell percentage and assignment probability of transcriptomic resemblance with *in vivo*
597 heart cells. **I.** UMAP plot of *in vivo* human developing heart cells and *in vitro* multilineage
598 organoid cells classified as atrial cardiomyocyte, subepicardial cells, fibroblast-like, smooth
599 muscle cells/fibroblast-like cells (probability greater or equal to 0.85). The UMAP projection
600 demonstrates that *in vitro* multilineage organoid cells align closely to the *in vivo* human heart
601 cells suggesting that the transcriptome of the multilineage organoid heart cells closely mimic that
602 of human developing heart cells, and favors atrial cardiomyocyte specification.
603

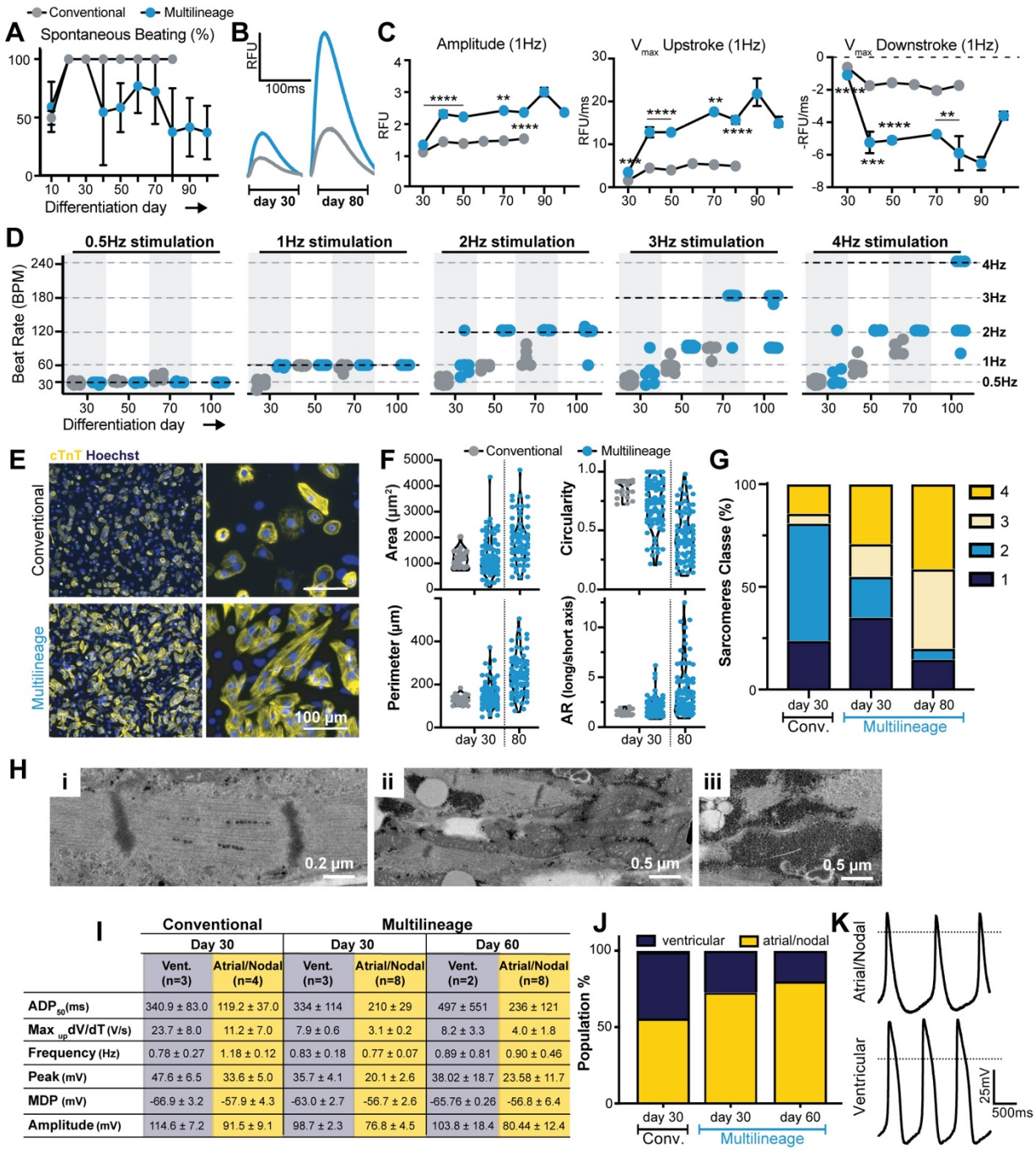

I

	Conventional		Multilineage			
	Day 30		Day 30		Day 60	
	Vent. (n=3)	Atrial/Nodal (n=4)	Vent. (n=3)	Atrial/Nodal (n=8)	Vent. (n=2)	Atrial/Nodal (n=8)
ADP_{50} (ms)	340.9 ± 83.0	119.2 ± 37.0	334 ± 114	210 ± 29	497 ± 551	236 ± 121
Max $_{up}$dV/dT (V/s)	23.7 ± 8.0	11.2 ± 7.0	7.9 ± 0.6	3.1 ± 0.2	8.2 ± 3.3	4.0 ± 1.8
Frequency (Hz)	0.78 ± 0.27	1.18 ± 0.12	0.83 ± 0.18	0.77 ± 0.07	0.89 ± 0.81	0.90 ± 0.46
Peak (mV)	47.6 ± 6.5	33.6 ± 5.0	35.7 ± 4.1	20.1 ± 2.6	38.02 ± 18.7	23.58 ± 11.7
MDP (mV)	-66.9 ± 3.2	-57.9 ± 4.3	-63.0 ± 2.7	-56.7 ± 2.6	-65.76 ± 0.26	-56.8 ± 6.4
Amplitude (mV)	114.6 ± 7.2	91.5 ± 9.1	98.7 ± 2.3	76.8 ± 4.5	103.8 ± 18.4	80.44 ± 12.4

Figure 4. Cardiomyocytes from multilineage organoids display phenotypic and functional maturation throughout culture, and preferentially specify into atrial/nodal-like cells. **A.** Multilineage organoids demonstrated a reduction in spontaneous beating throughout culture. **B.** Representative calcium flux traces at day 30 and 80 of culture. **C.** Cardiomyocytes in multilineage organoids display mature calcium flux features by showing higher amplitude, Vmax upstroke and downstroke (Conventional vs. Multilineage, **p<0.01, **p<0.005, ***p<0.001,

610 ****p<0.0001). **D.** Cardiomyocytes' ability to respond to electrical stimuli throughout culture
611 time. Black dashed line: electric stimuli applied**. E.** Representative immunofluorescence images
612 of dissociated cardiomyocytes from conventional microtissues and multilineage organoids. **F.**
613 Cardiomyocyte structural feature metrics. **G.** Cardiomyocyte sarcomere classification (from class
614 1—immature, undefined sarcomeres—to class 4—mature, parallel, striped sarcomeres). **H.** Day-
615 100 multilineage organoid cardiomyocyte sarcomeres (i), intercalated disks (ii, arrow heads) and
616 glycogen reservoir ultrastructure (iii). **I.** Electrophysiological characteristics of cardiomyocyte
617 subtypes. **J.** Percentage of ventricular and atrial/nodal cardiomyocytes dissociated from
618 conventional microtissues and multilineage organoids. **K.** Representative electrophysiological
619 traces of ventricular and atrial/nodal cardiomyocytes in multilineage organoids at day 30 of
620 culture.
621

622

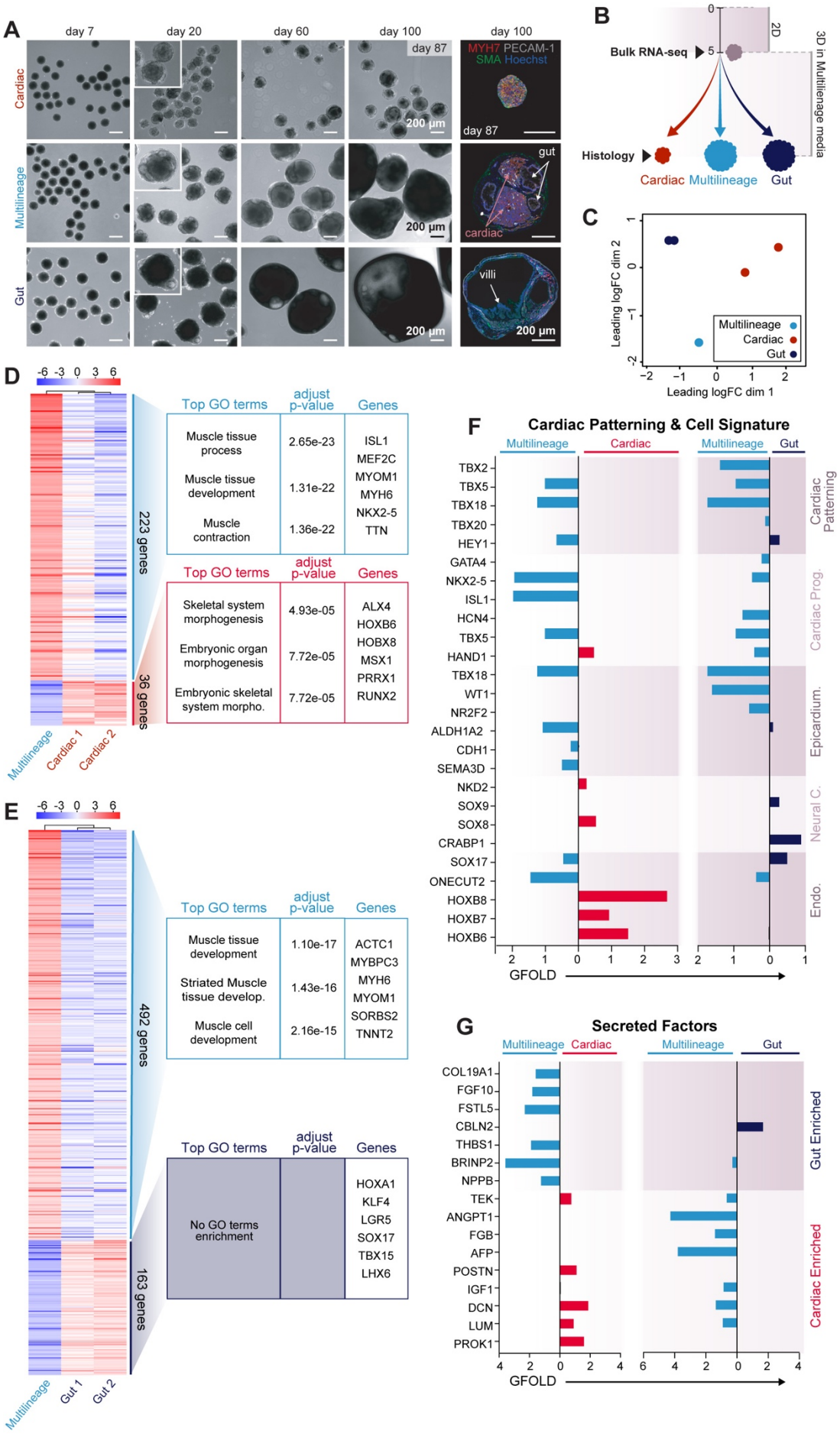
A
day 7
day 20
day 60
day 100
day 100
Cardiac
Multilineage
Gut
day 87
MYH7 PECAM-1
SMA Hoechst
200 µm
gut
cardiac
villi
B
Bulk RNA-seq
Histology
2D
3D in Multilineage media
Cardiac
Multilineage
Gut
C
Leading logFC dim 1
Leading logFC dim 2
Multilineage
Cardiac
Gut
D
223 genes
36 genes
Multilineage
Cardiac 1
Cardiac 2
Top GO terms
adjust p-value
Genes
Muscle tissue process
Muscle tissue development
Muscle contraction
2.65e-23
1.31e-22
1.36e-22
ISL1
MEF2C
MYOM1
MYH6
NKX2-5
TTN
Skeletal system morphogenesis
Embryonic organ morphogenesis
Embryonic skeletal system morpho.
4.93e-05
7.72e-05
7.72e-05
ALX4
HOXB6
HOBX8
MSX1
PRRX1
RUNX2
E
492 genes
163 genes
Multilineage
Gut 1
Gut 2
Muscle tissue development
Striated Muscle tissue develop.
Muscle cell development
1.10e-17
1.43e-16
2.16e-15
ACTC1
MYBPC3
MYH6
MYOM1
SORBS2
TNNT2
No GO terms enrichment
HOXA1
KLF4
LGR5
SOX17
TBX15
LHX6
F
Cardiac Patterning & Cell Signature
Multilineage
Cardiac
Gut
Cardiac Patterning
Cardiac Prog.
Epicardium.
Neural C.
Endo.
GFOLD
G
Secreted Factors
Gut Enriched
Cardiac Enriched
GFOLD

623 **Figure 5.** Multilineage organoid progenitor cells have a transcriptomic profile that supports the
624 co-development of cardiac and gut tissues. **A.** Mesendoderm progenitors cultured in AA medium
625 sometimes failed to develop into multilineage organoids, and instead yielded cardiac
626 microtissues or gut organoids. Brightfield and histological analysis revealed phenotypic diversity
627 between these outcomes. **B.** Experimental work flow schematic. **C.** Multidimensional scaling
628 (MDS) plot describes similarity between the progenitor cells that give rise to cardiac
629 microtissues and multilineage and gut organoids. **D.** Heat map of the pairwise comparison of
630 multilineage organoids and cardiac microtissues progenitors evidence a gene transcription profile
631 that favors muscle tissue formation. **E.** Heat map of the pairwise comparison of multilineage
632 organoid and gut organoid progenitors and respective GO terms and genes demonstrated that
633 multilineage progenitor gene expression supports cardiac tissue formation. **F-G.** Targeted
634 pairwise comparison for cell type-specific transcription factor (TF) genes (F) and secreted factor
635 genes (G) in multilineage vs. cardiac (left) and multilineage vs. gut (right) progenitor cells. The
636 multilineage organoid progenitors expressed key heart and endoderm-related TFs and secreted
637 factors highly expressed in gut organoid and cardiac microtissues progenitors.
638
639

Supplementary Materials for

Developmental co-emergence of cardiac and gut tissues modeled by human iPSC-derived organoids

A.C. Silva, O.B. Matthys, D.A. Joy, M.A. Kauss, V. Natarajan, M.H. Lai, D. Turaga, A.P. Blair, M. Alexanian, B.G. Bruneau, T.C. McDevitt

Correspondence to: todd.mcdevitt@gladstone.ucsf.edu

This PDF file includes:

- Materials and Methods (MM)
- Figure MM1
- Figs. S1 to S7
- Table S1 to S3
- Captions for Movies S1 to S8

Other Supplementary Materials for this manuscript include the following:

- Movies S1 to S8

668 **Materials and Methods**

669

670 *Human induced pluripotent stem cell culture*

671 WTC11 human induced pluripotent stem cells (iPSCs) genetically modified with fast green
672 fluorescent calcium indicator GCaMP6f (Huebsch *et al.*, 2015;Mandegar *et al.*, 2016) were
673 maintained on tissue culture plates coated with 80µg/mL growth factor-reduced (GFR) Matrigel
674 (Corning) and fed daily with mTeSR1 medium (StemCell Technologies). When the iPSCs
675 reached ~70% confluency, about every 3 days, they were dissociated to single cells using
676 Accutase (Innovative Cell Technologies) and re-plated at density of $1x10^4$ cells/cm^2 in mTeSR1
677 medium containing 10µM Y-27632 ROCK inhibitor (ROCKi; Selleckchem) for 24h.

678

679 *Differentiation to mesendoderm-derived progenitors*

680 GCaMP-WTC11 iPSCs were differentiated to mesendoderm-derived progenitor cells following a
681 chemically-defined, serum-free protocol modulating Wnt/β-catenin signaling (Lian *et al.*, 2012).
682 Briefly, iPSCs were seeded at a density of $3x10^4$ cells/cm^2 and fed with mTeSR1 medium until
683 100% confluency was reached (~3 days; termed differentiation day 0). At day 0, cells were fed
684 with RPMI1640 medium with B27 Supplement minus insulin (denoted as RPMI/B27-; Life
685 Technologies) supplemented with 12µM CHIR-99021 (Selleckchem). Exactly 24h later, the
686 medium was changed to fresh RPMI/B27-. On day 3, cells were fed with RPMI/B27-
687 supplemented with 5µM IWP2 (Sellekchem) for 48h. On day 5, cells were either dissociated for
688 tissue formation or fed with RPMI/B27- medium.

689

690

691

692 *Mesendoderm progenitor cell spheroid formation and culture*

693 Mesendoderm progenitor cells were dissociated at differentiation day 5 with Accutase and
694 aggregated as previous described (Hookway *et al.*, 2016). Briefly, dissociated cells in
695 RPMI/B27- medium with 10µM ROCKi were seeded into 800µm pyramidal agarose wells at a
696 density of $2.4x10^4$ cells/well. After 24h, cell spheroids were removed from the agarose wells by
697 gently pipetting using wide bore tips. Spheroids were maintained in rotary suspension culture at
698 a density of 65 spheroids/mL in 6-well low-attachment tissue culture plates (Hookway *et al.*,
699 2016). On day 7 of the differentiation protocol, 2 days after tissue aggregation, medium was
700 changed to either conventional cardiac-permissive medium, RPMI/B27+ (RPMI1640 medium
701 with B27 supplement with insulin; Life Technologies)(Lian *et al.*, 2012) or epicardial-permissive
702 medium (Advanced DMEM/F12 (Gibco) with 100µM L-Ascorbic Acid (Sigma))(Bao *et al.*,
703 2016) and refreshed every 3 days thereafter.

704

705 *Calcium imaging and functional analysis*

706 Calcium flux was analyzed by recording fluorescence of GCaMP signal in the spheroids. At day
707 30, 40, 50, 60, 70, 80, 90*, 100*, and 365*, conventional and multilineage microtissues (n = 4-
708 17 per condition) were equilibrated in Tyrode's solution (137 mM NaCl, 2.7 mM KCl, 1 mM
709 $MgCl_2$, 0.2 mM Na_2HPO_4, 12 mM $NaHCO_3$, 5.5 mM d-glucose, and 1.8 mM $CaCl_2$; Sigma-
710 Aldrich) for at least 30min at 37°C and then imaged on a Zeiss Axio Observer Z1 inverted
711 microscope equipped with a Hamamatsu ORCA-Flash 4.0 sCMOS camera. Electrical field
712 stimulation between 0.5Hz and 8Hz was applied with the MyoPacer (IonOptix) to evaluate
713 functional properties and eliminate differences in intrinsic beat rate between individual
714 spheroids. Calcium transients were recorded using Zen Professional software (v.2.0.0.0) with

715 10ms exposure and 100 frames per second. Circular regions of interest (ROI) with a diameter of
716 59.52 pixels were selected in the beating core of the spheroids and the mean fluorescence
717 intensity of the calcium transients was plotted against time. Additional metrics of calcium
718 handling properties, such as amplitude, stroke velocities, and beat rate, were analyzed using a
719 custom Python-script. Source code is available at https://github.com/david-a-joy/multilineage-
720 organoid (made public upon acceptance). *Of note, conventional samples were not evaluated at
721 these timepoints, because they were only viable until day 80 of culture.
722
723 *Calcium imaging with light sheet microscopy*
724 In order to assess calcium activity at higher resolution, light sheet fluorescence microscopy
725 (LSFM) was used to optically section live multilineage organoids and conventional microtissues
726 and record calcium transients *in situ* (Turaga *et al.*, 2020). Organoids/microtissues were
727 suspended in 1.5% low-melt agarose made up in Tyrode's solution in size 2 glass capillaries
728 (~1mm inner diameter; Zeiss). The Zeiss z.1 light sheet microscope used for imaging was
729 equipped with two PCO.edge sCMOS cameras, 10x 0.2 NA illumination lens, 20x 1.0 NA
730 detection lens, and 488nm laser, and the live samples were maintained at 37°C. 3D calcium
731 imaging stacks were acquired at ~120ms per frame and each z-spacing was 0.86µm per frame.
732 Single optical sections (3-4µm light thickness) were excited at 488nm and imaged at ~20Hz for
733 52 seconds (1000 total frames).
734
735 *Patch clamp analysis*
736 Conventional microtissues (n = 10 per condition), and multilineage organoids (n = 5-10 per
737 condition), as well as conventional 2D differentiated cardiomyocytes, were washed in PBS and

738 dissociated by successive 20min incubations in 0.25% Trypsin at 37ºC (1 incubation for
739 monolayers and maximum of 5 incubations for tissues) until complete dissociation to single
740 cells. Dissociated cells at a density of $0.03x10^6$cells/cm^2 were seeded onto GFR Matrigel-coated
741 glass coverslips for patch-clamp recordings in medium containing 10μM ROCKi. 24h after
742 seeding, cells were kept in culture media without ROCKi until the experiments began. To
743 conduct experiments, coverslips containing hiPSC-CMs were transferred to a heated RC-26
744 recording chamber (Warner Instruments), mounted to a Nikon inverted microscope and
745 continuously perfused with warmed Tyrode's solution. Experiments were performed at 35 ± 1ºC.
746 Action potentials were recorded from spontaneously beating cardiomyocytes using the perforated
747 patch technique with borosillicate glass pipettes (Sutter Instruments) with typical resistance of 2-
748 4 MΩ. The Tyrode's solution consisted of (in mM): 140 NaCl, 5.4 KCl, 1.8 $CaCl_2$, 1 $MgCl_2$, 10
749 glucose, and 10 HEPES, with the pH adjusted to 7.4 with NaOH. The patch pipette solution
750 consisted of (in mM): 150 KCl, 5 NaCl, 5 MgATP, 10 HEPES, 5 EGTA, 2 $CaCl_2$, and 240
751 μg/mL amphotericin B, with the pH adjusted to 7.2 with KOH. Data were acquired in current
752 clamp mode using an Axopatch 200B amplifier and Digidata 1440A digitizer coupled to pClamp
753 10 software (Molecular Devices). Data were digitized at 10 kHz and filtered at 1 kHz. Action
754 potential parameters were determined using Clampfit 10 software within pClamp. hiPSC-derived
755 cardiomyocytes were classified as either ventricular or nodal/atrial subtype after considering
756 multiple action potential parameters, including the APD_{90}/APD_{50} ratio, APD_{30-40}/APD_{70-80} ratio,
757 MDP, peak, amplitude, frequency, and dV/dT_{Max} (Ma *et al.*, 2011;Churko *et al.*, 2018).
758
759
760

761 *Cardiomyocyte structure analysis (area, perimeter, AR, circularity and sarcomere score)*

762 Day-30 and 80 conventional* (n =10 per condition) and multilineage microtissues (n = 5-10 per
763 condition) were dissociated into single cells as described above (patch clamp analysis sections)
764 and seeded onto GFR Matrigel-coated glass coverslips. 24h post-seeding, the cells were fed with
765 fresh medium without ROCKi for at least 48h to allow the cells to acquire their natural
766 morphology. Coverslips were then fixed in 4% paraformaldehyde (EMS), stained with the
767 cardiomyocyte-specific marker cardiac Troponin T (cTnT), labeled with Hoechst to detect
768 nuclei, and mounted on glass slides using ProLong™ Gold Antifade Mountant (ThermoFisher
769 Scientific). Representative images were acquired for each sample condition using an inverted
770 microscope (Zeiss Axio Observer Z1). For each cell, area, perimeter, circularity, and aspect ratio
771 (AR) were quantified using Fiji software. In addition, each cardiomyocyte was assigned a score
772 for sarcomere development between 1 and 4, defined as: 1) unaligned sarcomeres and absence of
773 a striped pattern; 2) continuous sarcomeres, well ordered but not in parallel; 3) continuous
774 sarcomeres, organized mostly in parallel, but with less-defined striped pattern; 4) continuous
775 sarcomeres with striped pattern, organized mostly in parallel **(Figure M1)**(Nguyen *et al.*,
776 2014;Judge *et al.*, 2017). The percentage of cells in each class of sarcomere development was
777 calculated per sample and timepoint. * Of note, conventional samples were not evaluated at day
778 80, because only a few microtissues were available and viable at this later stage.

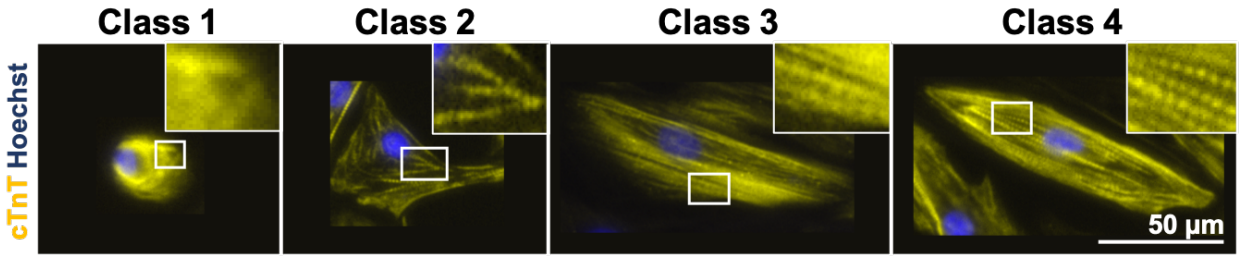

779 **Figure M1.** Representative images of the different classes of sarcomere development.

780 *Histology, immunostaining, and in situ hybridization*

781 Conventional microtissues (n=10 per condition), cardiac organoids (n=10 per condition),
782 multilineage organoids (n=5-10 per condition), and gut (n=5-10 per condition) organoids were
783 fixed in 10% neutral buffered formalin (VWR) with 0.03% eosin (Newcomer Supply) at room
784 temperature for 1h and washed with PBS. Samples were embedded in HistoGel Specimen
785 Processing Gel (ThermoFisher Scientific), paraffin processed and embedded, cut into 5µm
786 sections, and adhered to positively charged glass slides. Slides were then deparaffinized with
787 xylene, re-hydrated through a series of decreasing ethanol concentrations (100%, 100%, 95%,
788 80%, 70%), and rinsed in tap water. Hematoxylin and eosin (H&E), Russell-Movat
789 Pentachrome, and Safranin O stainings were performed according to manufacturer's instructions
790 and the slides were mounted with Cytoseal 60 (Richard-Allan Scientific) and glass coverslips.
791 For immunofluorescence staining, heat-induced epitope retrieval was performed by immersing
792 slides in Tris-EDTA buffer (Cellgro) pH 9.0 or citrate buffer (Vector Laboratories) pH 6.0 in a
793 95°C water bath for 35min. Slides were cooled for 20min at RT and washed 3x with PBS.
794 Samples were permeabilized by slide immersion in 0.2% or 0.5% Triton X-100 (Sigma) in PBS,
795 washed 3x in PBS, and blocked in 1.5% normal donkey serum (NDS; Jackson
796 ImmunoResearch). Primary and secondary antibody cocktails were diluted in blocking solution
797 **(Table S3)**. 3 PBS washes were performed after primary (overnight, 4°C) and secondary
798 antibody (1h, RT) incubations. For in situ hybridization analysis, RNAscope Multiplex
799 Fluorescent Reagent Kit v2 was used on paraffin sections, following user manual #323100-USM.
800 Human RNAscope probes used in this study were: WT1-C2 (catalog #415581); FOXA2-C1
801 (catalog #832221); TBX18-C3 (catalog #832231). Nuclei were counter-labeled with Hoechst and

802 coverslips were mounted on slides using ProLong™ Gold Antifade Mountant. Samples were
803 imaged on the Zeiss Axio Observer Z1.
804
805 *Whole-mount immunostaining*
806 Conventional microtissues (n=5) and multilineage organoids (n=5) were fixed in 4%
807 paraformaldehyde at room temperature for 1h with agitation (40 rpm). Samples were then
808 washed 3x in stain buffer (2% NDS, 0.1% Tween-20 (Sigma-Aldrich) in PBS) and
809 permeabilized for 30min in 1.5% Triton X-100, followed by a 3h incubation in blocking buffer
810 (3.5% NDS, 0.1% Tween-20 in PBS). Microtissues/organoids were incubated with TBX18 and
811 cTnT primary antibodies overnight at 4ºC and secondary antibodies plus phalloidin and Hoechst
812 stains for 4h at RT **(Table S3)**, followed by 3 final washes in stain buffer prior to imaging.
813
814 *Whole-spheroid structural analysis by light sheet microscopy*
815 Whole-mount immunostained conventional microtissues and multilineage organoids were
816 suspended in 1.5% low-melt agarose (made up in PBS; IBI Scientific) in size 2 glass capillaries
817 immediately prior to imaging. Microtissues/organoids were each imaged at three angles (120°
818 rotations between views), and then stitched with multi-view reconstruction to provide isotropic
819 resolution throughout the sample, as previously described (Turaga *et al.*, 2020). Volumetric
820 reconstruction and size analyses were performed using Imaris 8.3 software.
821
822 *Single-cell RNA sequencing*
823 Multilineage and gut organoids at day 100 of culture (n = 5-8) were washed in PBS and
824 dissociated by successive 20-min incubations in 0.25% trypsin at 37ºC (maximum of 5

825 incubations) until complete dissociation to single cells. 10,000 cells in PBS supplemented with
826 0.08% FBS were prepared for sequencing by droplet encapsulation using the Chromium
827 Controller and library preparation with the 10x Genomics Single Cell 3' v2 Library and Gel
828 Bead Kit (10x Genomics). Libraries were sequenced using the NovaSeq S4 (Illumina) to a
829 minimum depth of 50,000 mean reads per cell. Sequences were demultiplexed and aligned to
830 human reference genome grch38 using *CellRanger* v3.0.2, and downstream analysis was
831 performed with Seurat v.3.1. Cells with fewer than 1,500 genes were excluded from analysis and
832 cell identity was assigned to each cluster by cross-referencing cluster marker genes with known
833 cardiac and gut markers. Cell-cycle did not introduce heterogeneity in scRNA-seq data. Raw
834 data is available at Geo under the accession number GSE153075 (access token:
835 qvslsuecdpofjup).
836
837 *Classification of In Vivo Cardiac Cell Types*
838 To evaluate the transcriptomic similarity between multilineage organoid heart cells and human
839 fetal heart cells, an *in vivo* heart cell classifier was applied. A multiclass logistic regression (lr)
840 model was trained on *in vivo* cardiac cell types(Asp *et al.*, 2019). To have consistent features, we
841 ran SCTransform (default, version 3.1.5.9) independently on each dataset and then took an
842 intersection of their top 3,000 highly variable genes. A total of 1,418 genes, transformed as
843 Pearson residuals, were used to train the model. The resulting expression matrix of 3,717 single
844 cells from a 6.5–7 post conception week (PCW) heart with established cardiac cell types was
845 used to train the model using a 'sag' solver and cross-entropy loss cost function with the Python
846 package sklearn (version 0.22.2.post1).

847 A two-dimensional UMAP (version 0.4.4) latent space was fit to *in vivo* subepicardial cells,
848 fibroblast-like, smooth muscle cells/fibroblast-like, and atrial cardiomyocytes. We used the lr
849 model's feature space for UMAP dimensionality reduction. A sklearn C-support vector classifier
850 was then trained on the four *in vivo* cell types using the UMAP latent space. *In vitro* cells that the
851 lr model classified as one of the four *in vivo* cell types, with probabilities greater than or equal to
852 eighty-five percent, were transformed into the UMAP latent space. The trained C-support vector
853 classifier was then applied to the *in vitro* cell's UMAP transform embedding. The Seaborn
854 (version 0.10.1) library was used to visualize UMAP transformations.
855
856 *Bulk RNA sequencing*
857 To reduce batch effects between RNA-sequencing analysis of the mesendoderm-derived
858 progenitors between experiments, bulk RNA-sequencing was applied. Day 5 progenitor cells that
859 gave rise to cardiac (n=2), multilineage (n=1), or gut organoids (n=2) were lysed with Trizol
860 (Ambion) and RNA was extracted using the Direct-zol Miniprep kit (ZymoResearch) and
861 quantified using the NanoDrop 2000c (ThermoFisher Scientific). RNA-seq libraries were created
862 using the SMARTer Stranded Total RNA Sample Prep Kit (Takara Bio) and sequenced using
863 NextSeq500/550 High Output v2.5 kit (spiked with 10% PhiX; Illumina) to a minimum depth of
864 29 million reads per sample. The sequences were aligned to grch38 using HiSat2 (Kim *et al.*,
865 2019), reads were quantified using featureCounts (Liao *et al.*, 2014), and differential expression
866 was determined using GFOLD(Feng *et al.*, 2012). Relative gene expression level was determined
867 using the "l" normalization algorithm (Zhang *et al.*, 2019). Raw data is available at Geo under
868 the accession number GSE153071 (access token: utwxqsawhjcpfgz).
869

870 *Statistical analysis*

871 All results were obtained in three independent experiments, unless otherwise stated, and shown
872 as mean ± standard error of the mean (SEM). The statistical analysis of the data was performed
873 using Prism 8 with statistical significance determined at $p < 0.05$. Tukey's multiple comparison
874 test was applied. Whenever normality was verified through D'Agostino-Pearson omnibus
875 normality test, the t-Student test was applied and the Independent Samples Mann-Whitney U test
876 was used for the remaining analyses. A blinded approach (labeling samples with an
877 alphanumeric code) was implemented for analyzing cardiomyocyte morphological features (area,
878 perimeter, AR, circularity, sarcomere scoring), patch clamp, histology, and immunostaining.
879

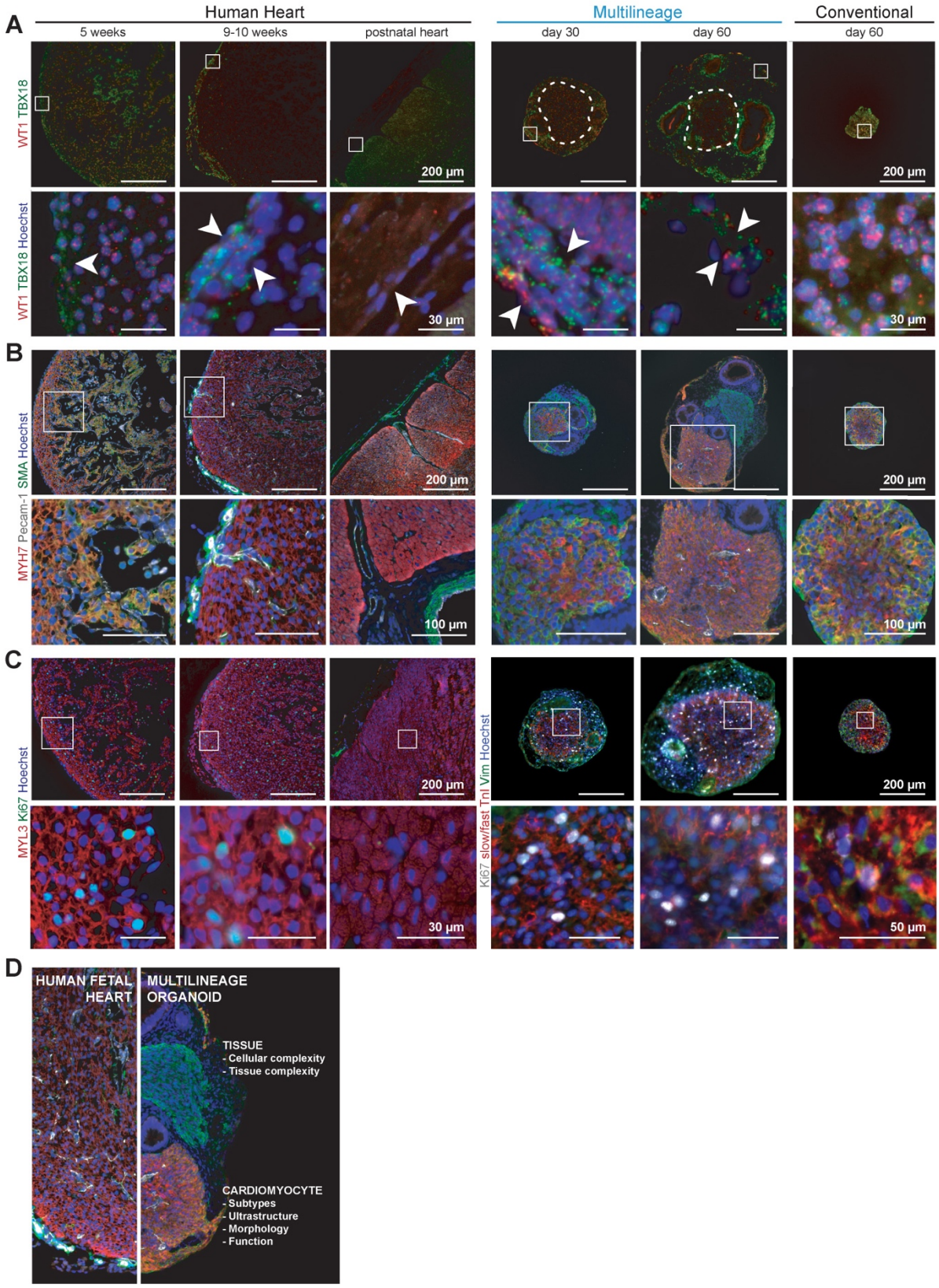

880 **Figure S1**. *Related to Figure 1 and 2.* Comparison of conventional and multilineage

881 microtissues with human heart development (**A-B**). **A.** RNAscope validation of TBX18 and WT1
882 transcripts in native human heart tissue, multilineage organoids, and conventional microtissues.
883 Dashed line denotes boundary of the cardiac core. **B.** Identification of cardiomyocytes
884 (MYH7+SMA-, MYH7+SMA+), smooth muscle cells (SMA+MYH7-), and endothelial cells
885 (Pecam-1+) in native human heart tissue, multilineage organoids, and conventional microtissues.
886 **C.** Proliferating cardiomyocytes in human ventricle wall tissue (MYL3+Ki67+), multilineage
887 organoids, and conventional microtissues (slow/fast TnI+Ki67+). **D.** Comparative images
888 exhibiting similarities between the cardiac compartment of native human fetal heart tissue and
889 that of the multilineage organoids.
890

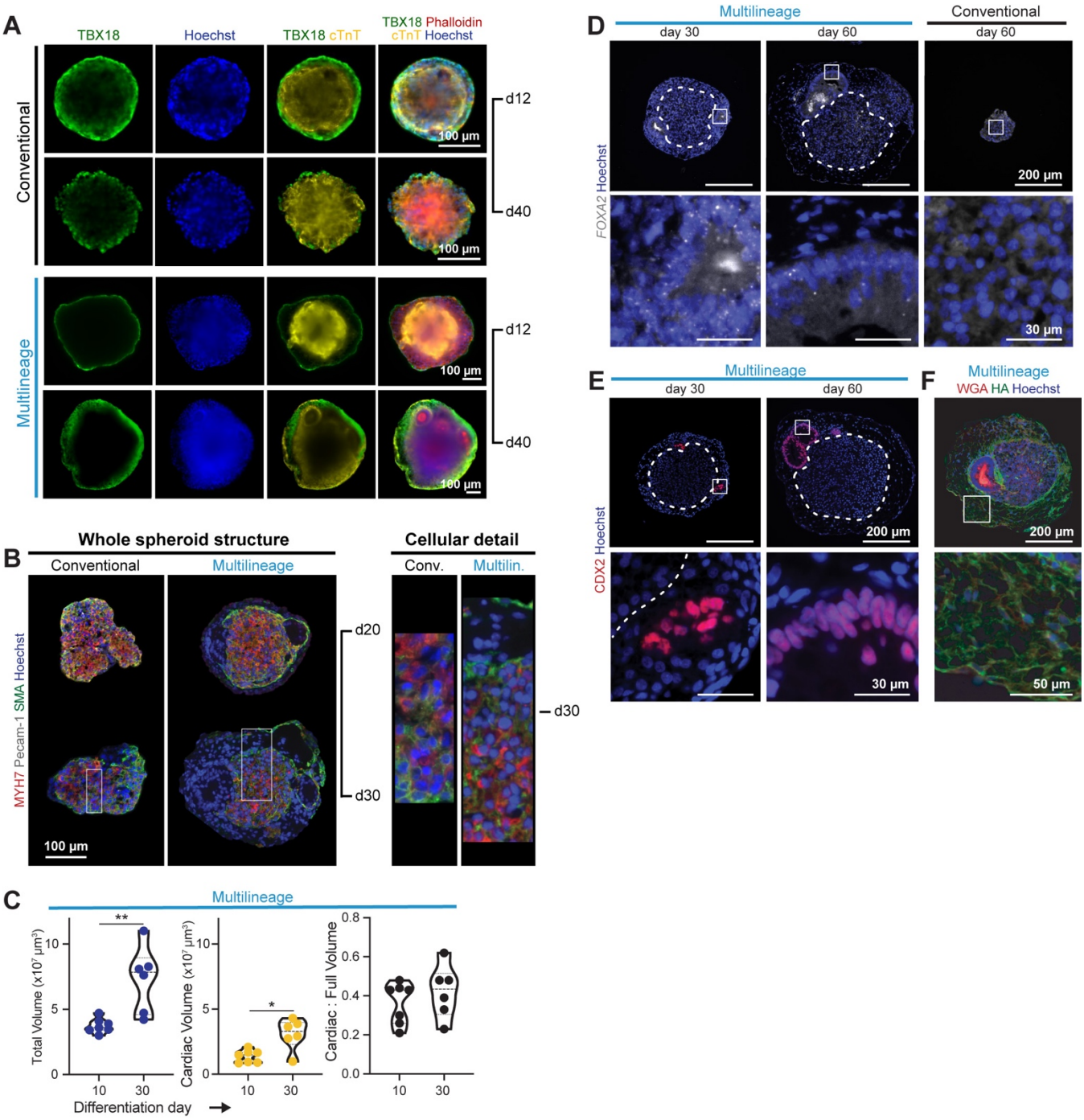

891

892 **Figure S2.** *Related to Figure 1 and 2.* Multilineage organoid histological and volumetric
893 analysis**. A.** Detailed light-sheet images of the epicardial layer (TBX18+) of conventional and
894 multilineage microtissues. **B.** Conventional and multilineage microtissues demonstrate the
895 presence of cardiomyocytes (MYH7+), smooth muscle cells (SMA+) and MYH7+/SMA+
896 cardiomyocytes (d20, more immature). **C.** Total volume (blue), cardiac core volume (yellow),

897 and ratio of cardiac:total volume (black) of the multilineage organoids at days 10 and 30 of
898 culture. *$p<0.05$, **$p<0.005$. **D-E.** Epithelial-like structures in multilineage organoids
899 correspond to primitive midgut based on the detection of FOXA2 transcript by RNAscope (D)
900 (absent in conventional microtissues) and CDX2 protein by immunostaining (E). **F.** Hyaluronic
901 acid (HA) is expressed in the interstitial tissue (tissue surrounding the cardiac core and the gut)
902 in the multilineage organoids. White squares regions in high magnification at the bottom panels.
903 Dashed line boundary of the cardiac core and gut.
904

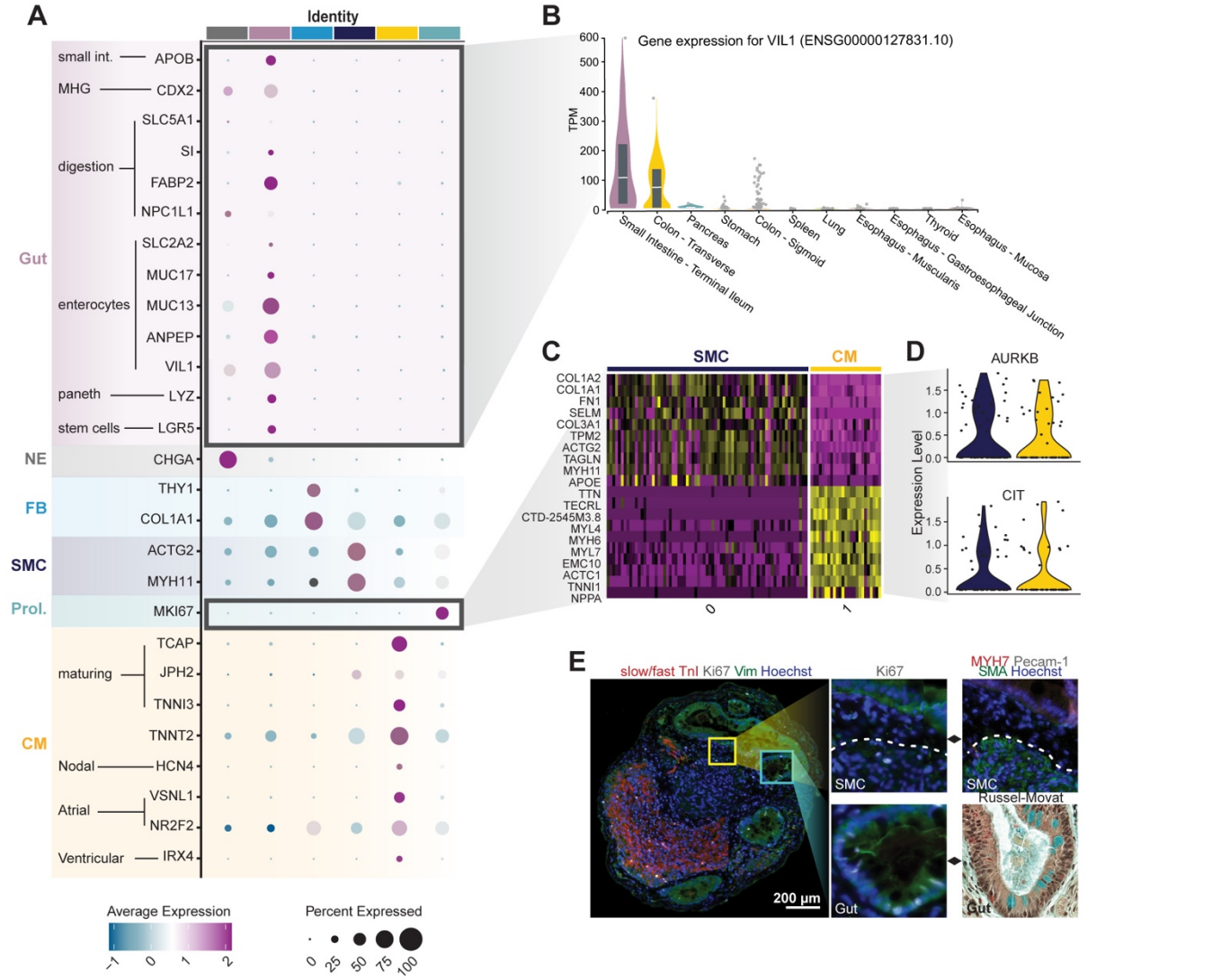

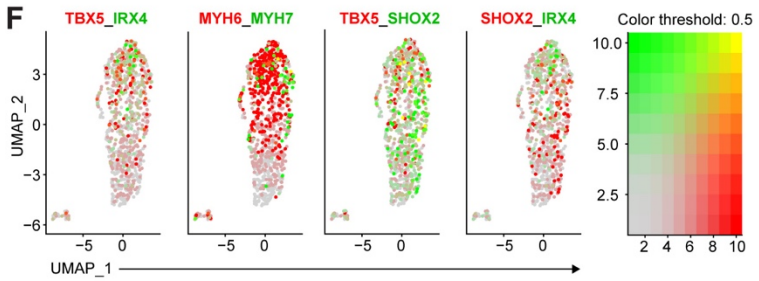

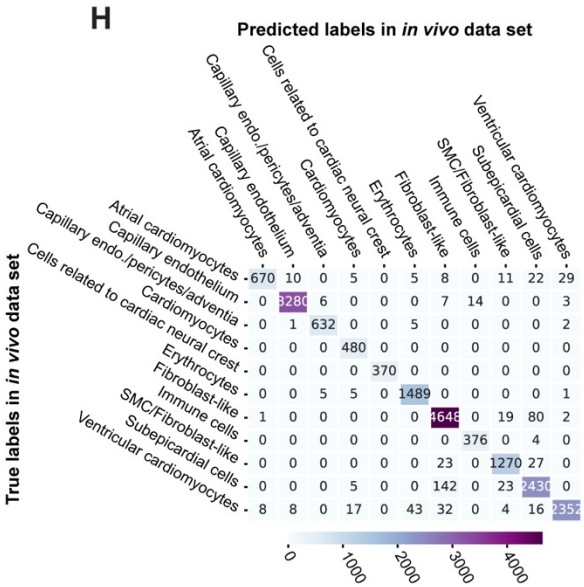

G

Cell Identity	Cell Number	% Cardiomyocyte
Atrial CM	1201	98.44
Ventricular CM	13	1.07
Cardiomyocytes	6	0.49
Fibroblast-like	1322	-
SMC/Fibroblast-like	344	-
Subepicardial cells	99	-
Cappilary endothelium/ pericytes/adventia	4	-
Cappilary endothelium	2	-
Erythrocytes	21	-

905

906 **Figure S3.** *Related to Figure 3.* Transcriptional characterization of day-100 multilineage
907 organoids. **A.** Dotplot of key genes that define cell type identity of UMAP clusters as
908 cardiomyocytes (CM), proliferating cells (Prol.), smooth muscle cells (SMC), fibroblasts (FB),
909 enteroendocrine cells (EnteroE), and gut. **B.** Violin plot of VIL1 expression across different
910 endoderm-derived tissues using GTEx tissue dataset (https://www.gtexportal.org/). **C.** Heatmap
911 of secondary analysis of re-clustered proliferating cells identified SMCs (cluster 0) and CMs
912 (cluster 1) as the main proliferative cell types at day 100. **D.** Violin plot of key karyokinesis-
913 related genes in proliferating SMCs and CMs. **E.** Histological validation of SMC proliferation
914 (yellow square; ki67+, SMA+) and gut cell proliferation (blue square; ki67+, Russel-Movat) in a
915 day-100 multilineage organoid. Dashed line denotes SMC region. **F.** Feature plot showing co-
916 expression of key atrial, ventricular and pacemaker related genes in day-100 organoids. **G.** Table
917 showing the distribution of organoid heart cells classified to various cell identities by the *in vivo*
918 cell classifier. **H.** Confusion matrix comparing test vs. predicted cell type labels for human
919 developing fetal cardiac cells(Asp *et al.*, 2019).
920

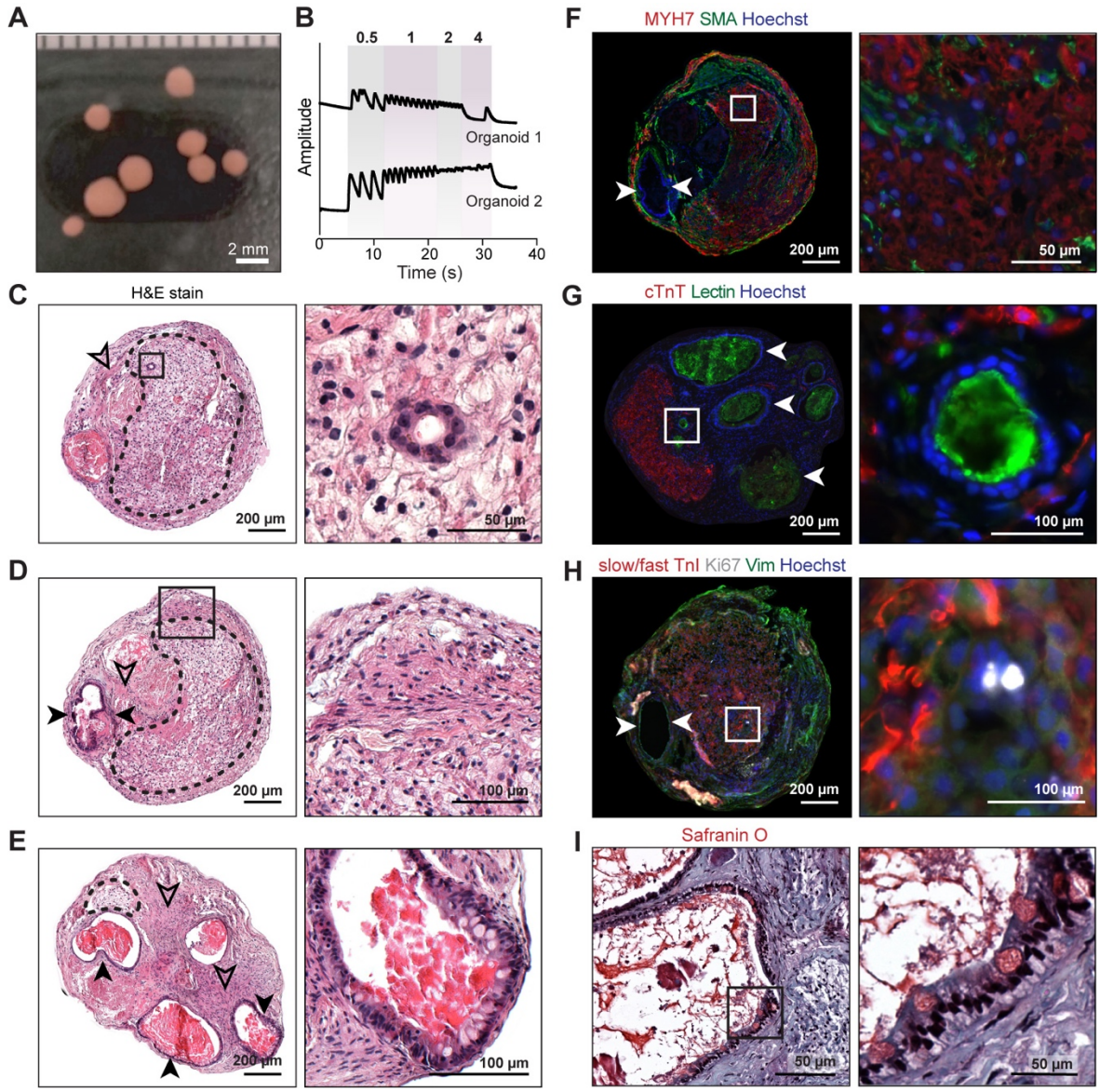

921

922 **Figure S4.** *Related to figure 2.* 1 year-old multilineage organoids. **A.** Macroscopic field of view
923 of multiple 1 year-old organoids. **B.** Calcium handling response to electrical stimulation (0.5-
924 4Hz). **C-E.** Hematoxylin and eosin stain (H&E) reveals vasculature-like structures (**C**), smooth
925 muscle cells (**D**), and intestine (**E**). Dashed line denotes cardiac core; solid arrowhead indicates
926 gut; outlined arrowhead indicates smooth muscle cells. **F.** Immunostaining highlights the
927 presence of cardiomyocytes (MYH7+) and smooth muscle cells (SMA+). **G.** Lectin-positive
928 vasculature-like structures are found close to the cardiac compartment (inset) and non-specific
929 lectin expression was also identified in gut structures (solid arrowheads). **H.** Identification of

930 actively proliferating cells by Ki67+ immunostaining. **I.** Safranin O staining reveals presence of
931 goblet cells (counterstained in red) in the gut structures.
932

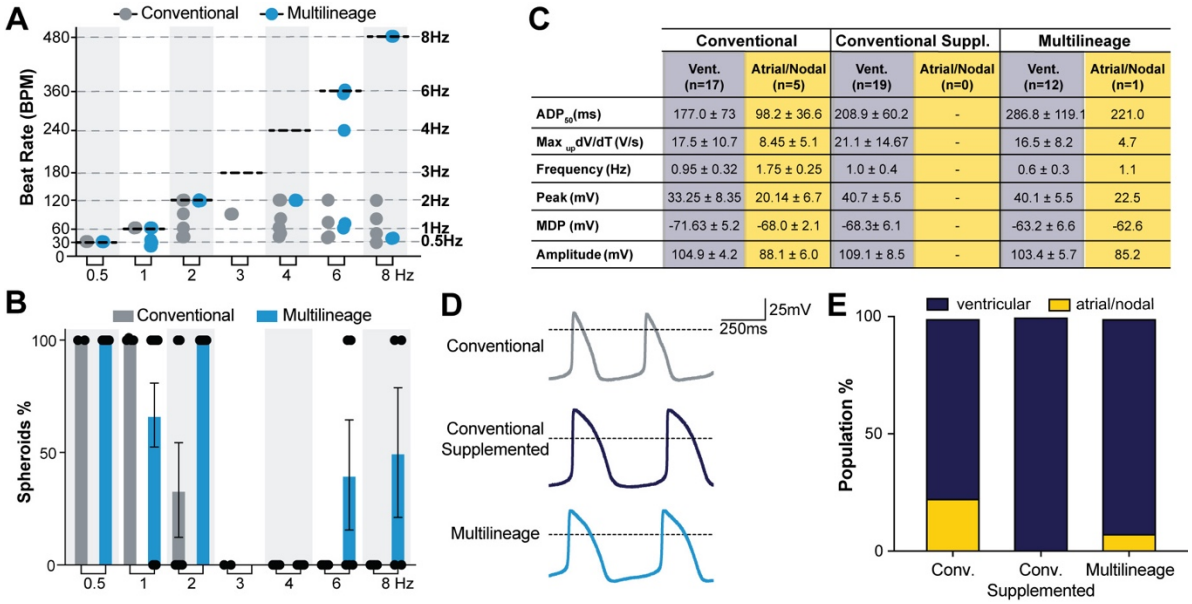

	Conventional		Conventional Suppl.		Multilineage	
	Vent. (n=17)	Atrial/Nodal (n=5)	Vent. (n=19)	Atrial/Nodal (n=0)	Vent. (n=12)	Atrial/Nodal (n=1)
ADP_{50}(ms)	177.0 ± 73	98.2 ± 36.6	208.9 ± 60.2	-	286.8 ± 119.1	221.0
Max_{up}dV/dT (V/s)	17.5 ± 10.7	8.45 ± 5.1	21.1 ± 14.67	-	16.5 ± 8.2	4.7
Frequency (Hz)	0.95 ± 0.32	1.75 ± 0.25	1.0 ± 0.4	-	0.6 ± 0.3	1.1
Peak (mV)	33.25 ± 8.35	20.14 ± 6.7	40.7 ± 5.5	-	40.1 ± 5.5	22.5
MDP (mV)	-71.63 ± 5.2	-68.0 ± 2.1	-68.3± 6.1	-	-63.2 ± 6.6	-62.6
Amplitude (mV)	104.9 ± 4.2	88.1 ± 6.0	109.1 ± 8.5	-	103.4 ± 5.7	85.2

Figure S5. *Related to Figure 4.* Cardiomyocyte functional analyses. **A.** Calcium handling response of day 80 conventional and multilineage spheroids subjected to electrical field stimulation at increasing frequencies (0.5-8Hz). **B**. Percentage of conventional and multilineage spheroids capable of responding to the electrical field (0.5-8Hz) stimulation applied at day 80 of culture. **C.** Table displaying electrophysiological properties of day-30 cardiomyocytes differentiated in 2D in various media conditions: conventional media (RPMI/B27+, Ca^{2+}=0.42mM), conventional media supplemented with ascorbic acid (AA) and calcium (Conventional Suppl., AA=100 µg/ml, Ca^{2+}=0.63mM) and multilineage-permissive media (AA=100 µg/ml, Ca^{2+}=1.05mM). **D.** Representative traces of ventricular cardiomyocytes in the different media conditions. **E.** Percentage of ventricular and atrial/nodal cardiomyocytes across the different media conditions.

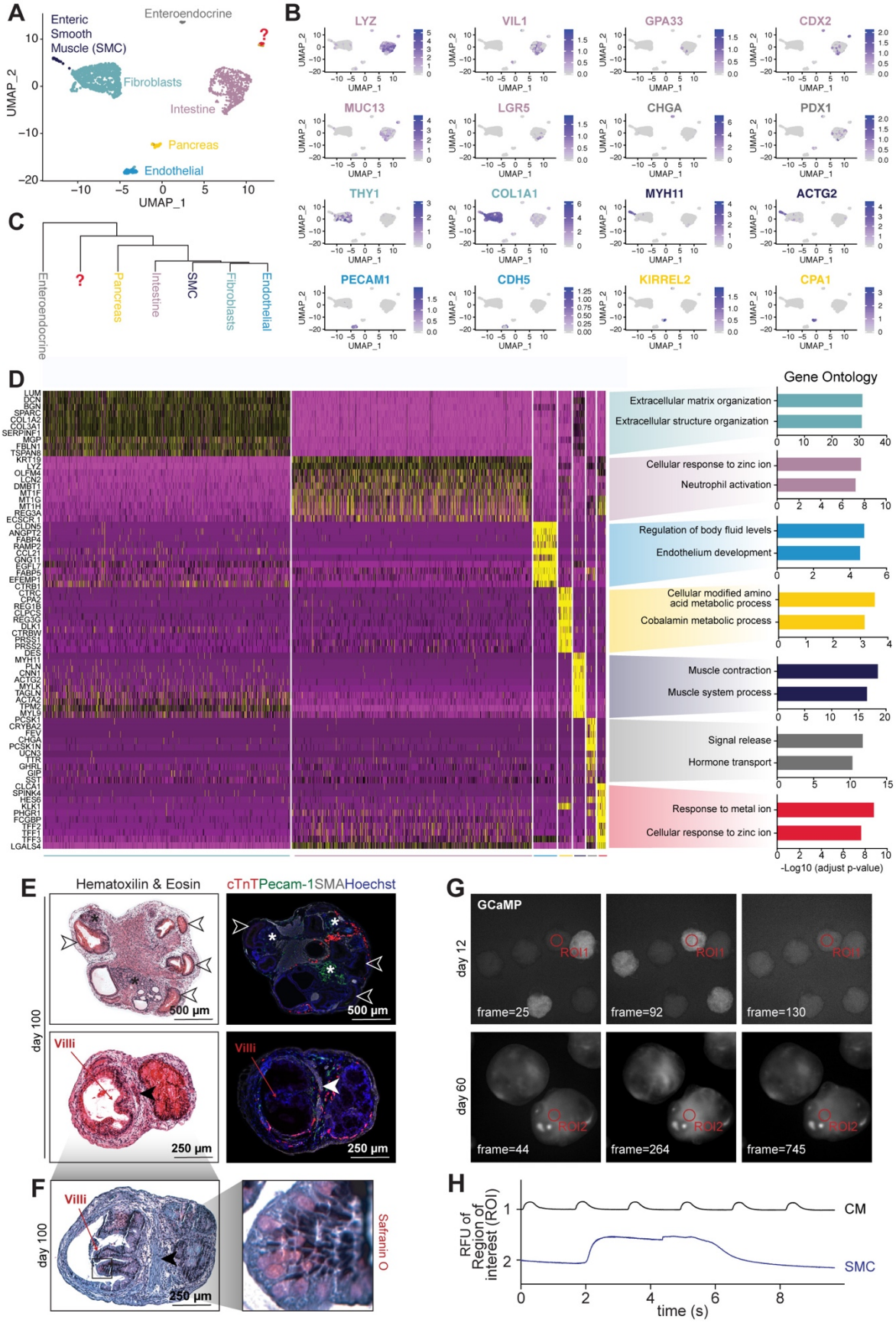
A
Enteric Smooth Muscle (SMC)
Enteroendocrine
?
Fibroblasts
Intestine
Pancreas
Endothelial
UMAP_2
UMAP_1
B
LYZ
VIL1
GPA33
CDX2
MUC13
LGR5
CHGA
PDX1
THY1
COL1A1
MYH11
ACTG2
PECAM1
CDH5
KIRREL2
CPA1
C
Enteroendocrine
?
Pancreas
Intestine
SMC
Fibroblasts
Endothelial
D
Gene Ontology
Extracellular matrix organization
Extracellular structure organization
Cellular response to zinc ion
Neutrophil activation
Regulation of body fluid levels
Endothelium development
Cellular modified amino acid metabolic process
Cobalamin metabolic process
Muscle contraction
Muscle system process
Signal release
Hormone transport
Response to metal ion
Cellular response to zinc ion
-Log10 (adjust p-value)
E
Hematoxilin & Eosin
cTnTPecam-1SMAHoechst
day 100
500 µm
Villi
250 µm
F
Villi
day 100
250 µm
Safranin O
G
GCaMP
day 12
day 60
ROI1
ROI2
frame=25
frame=92
frame=130
frame=44
frame=264
frame=745
H
RFU of Region of interest (ROI)
CM
SMC
time (s)

945

946 **Figure S6.** *Related to Figure 5.* Analysis of day-100 gut organoids by single-cell RNA
947 sequencing, histology, and immunostaining. **A.** UMAP plot colored by cell identity. **B.** Feature
948 plot of key genes used to assign cell-type identity to UMAP clusters. **C.** Hierarchical clustering
949 of the different UMAP cell populations. **D.** Heatmap of top 10 differentially expressed genes that
950 define each UMAP cluster with associated biological process gene ontology analysis. **E-F.**
951 Histological analysis of gut organoids from 2 independent experiments. Hematoxylin & eosin
952 staining (left, E), immunostaining to identify the presence of endothelial cells (Pecam-1+),
953 smooth muscle cells (SMA+, solid arrowhead), and remnant cardiomyocytes (cTnT+) (right, E)
954 and Safranin O staining to identify the presence of goblet cells (red, F). Outlined arrowhead,
955 intestine tissue; *, pancreas-like tissue. **G-H.** Representative images of spontaneous calcium flux
956 transients (G) in gut organoids at day 12 (top, ROI1) and 60 (bottom, ROI2) of culture and
957 respective ROIs traces (H) (Movie S8).
958

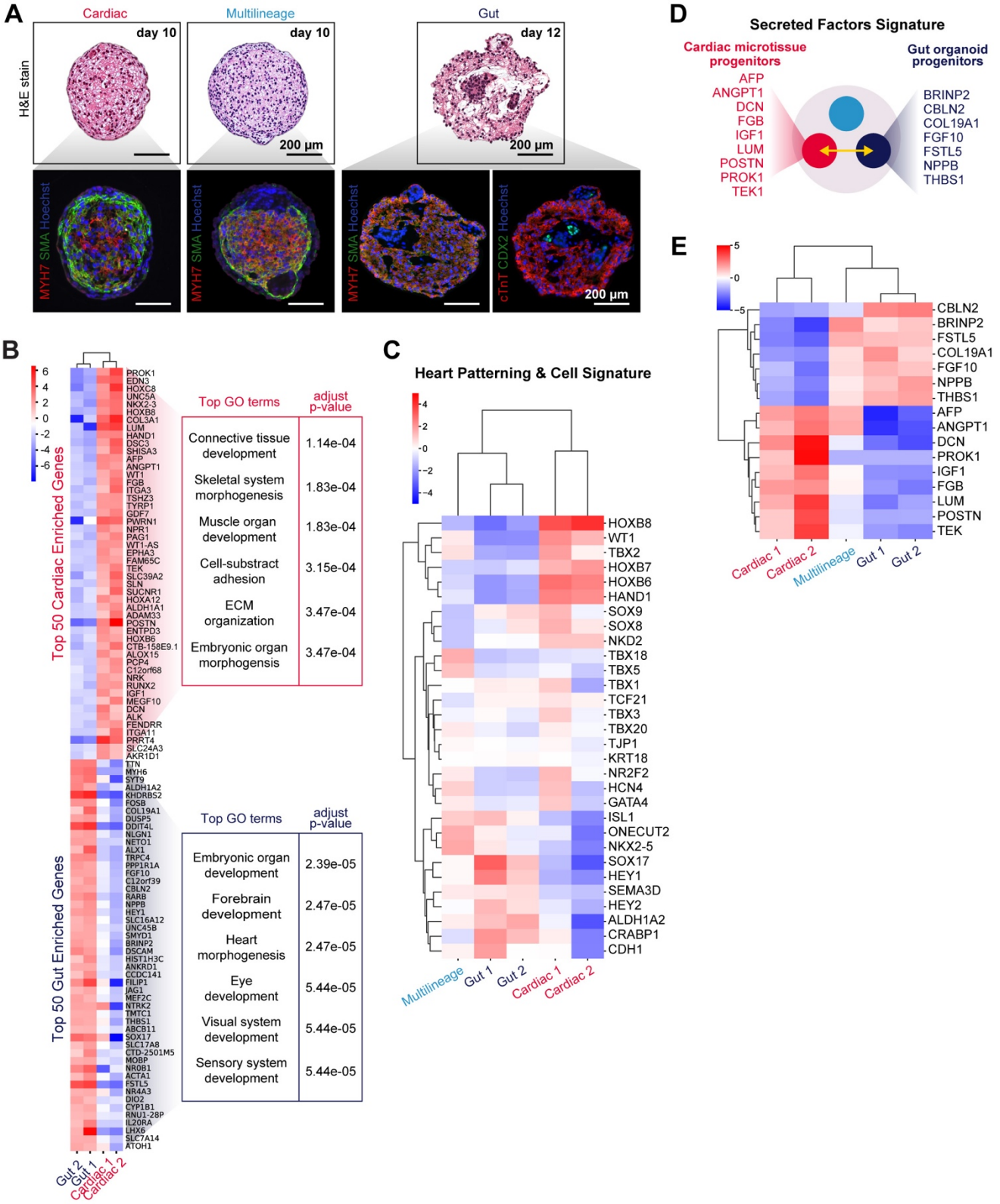

959 **Figure S7.** *Related to Figure 5.* Transcriptional variability of the progenitor populations across
960 experiments. **A.** Spheroid phenotype diversity observed across experiments at early stages of

961 culture. **B.** Heat map and respective gene ontology (GO) terms analysis of cardiac microtissues
962 (top) versus gut organoids progenitors (bottom). **C.** Heatmap of the differentially expressed
963 genes analyzed through a target analysis of relevant cardiac- and gut-related genes in the
964 progenitor cell populations between experiments. **D.** List of highly expressed genes encoding
965 secreted factors in cardiac microtissues and gut organoids. **E.** Heatmap of the differentially
966 expressed genes detailed in (**D**) in the progenitor cell populations for each experiment.
967

968 **Table S1.** List of genes that describe each cell cluster identity derived from Seurat analysis.

969

970 **Table S2.** *In vivo* cell classifier gene features and weights for each cell type prediction.

971

972 **Table S3.** Panel of dyes, primary and secondary antibodies used for whole mount

973 immunostaining, immunocytochemistry and paraffin sections.

974

Protein	**Source**	**Catalog #**	**Dilution**
Alexa Fluor 488 Donkey anti-mouse IgG	Invitrogen		1:400
Alexa Fluor 555 Donkey anti-rabbit IgG	Invitrogen		1:400
Alexa Fluor 647 Donkey anti-goat IgG	Invitrogen		1:400
Alexa Fluor 647 Phalloidin	Invitrogen	A22287	1:100
CDX2	R&D Systems	AF3665	1:100
Collagen IV	Millipore	AB769	1:100
Ki67	Invitrogen	Ab15580	1:500
Smooth muscle actin	DAKO	M0851	1:100
HABP	Sigma-Aldrich	H9910	1:65
Hoechst 33342	Thermo Scientific	62246	1:10000
MYL3	Abcam	Ab680	1:1200
MYH7	Sigma-Aldrich	HPA001239	1:100
MLC2-v	Abcam	Ab79935	1:200
PECAM-1	Santa Cruz	SC-1506	1:1000
TBX18	R&D Systems	MAB63371	1:100
To-Pro-3 Iodide	Thermo Fisher	T3605	1:5000
Troponin I Slow and Fast	Abcam	ab110132	1:100
Troponin T	Abcam	ab45932	1:400
Vimentin	Millipore	AB1620	1:100
WGA	Thermo Fisher	AF350	1:100

975

976

977 **Movie S1.** Spontaneous calcium transients, depicted by GCaMP fluorescence signal, of day-30
978 conventional microtissues.

979 **Movie S2.** Spontaneous calcium transients of day-30 multilineage microtissues.

980 **Movie S3.** Representative 3D reconstruction of day-12 multilineage microtissue by light sheet
981 microscopy. Total volume was quantified based on a nuclear label (blue, Hoechst) and volume of
982 the cardiac core was based on cardiomyocyte-specific marker, cardiac troponin T (yellow,
983 cTnT). Stromal-like cell population identified by phalloidin stain (red).

984 **Movie S4.** Representative 3D reconstruction of day-30 multilineage microtissue by light sheet
985 microscopy, with Hoechst labeling nuclei (blue) and cTnT marking cardiomyocytes (yellow).
986 Stromal-like cell population identified by phalloidin stain (red).

987 **Movie S5.** Lightsheet microscopy-based acquisition of the rhythmic calcium flux transients of
988 cardiomyocytes in day-30 multilineage organoids in the absence of electrical stimulation.

989 **Movie S6**. Lightsheet microscopy-based acquisition of the rhythmic and sporadic calcium flux
990 transients from cardiomyocytes and smooth muscle cells, respectively, in day-76 multilineage
991 organoids in the absence of electrical stimulation.

992 **Movie S7.** Calcium transients of 1-year-old multilineage organoids subjected to electrical
993 stimulation from 0.5-4Hz.

994 **Movie S8.** Calcium transients of day-12 and day-60 gut organoids.
995

996 **References:**
997

998 Al Alam, D., Danopoulos, S., Schall, K., Sala, F. G., Almohazey, D., Fernandez, G. E., Georgia,
999 S., Frey, M. R., Ford, H. R., Grikscheit, T.*, et al.* 2015. Fibroblast growth factor 10 alters
1000 the balance between goblet and Paneth cells in the adult mouse small intestine. *Am J*
1001 *Physiol Gastrointest Liver Physiol,* 308**,** G678-90.
1002 Anderson, C., Khan, M. a. F., Wong, F., Solovieva, T., Oliveira, N. M. M., Baldock, R. A.,
1003 Tickle, C., Burt, D. W. andStern, C. D. 2016. A strategy to discover new organizers
1004 identifies a putative heart organizer. *Nat Commun,* 7**,** 12656.
1005 Asp, M., Giacomello, S., Larsson, L., Wu, C., Furth, D., Qian, X., Wardell, E., Custodio, J.,
1006 Reimegard, J., Salmen, F.*, et al.* 2019. A Spatiotemporal Organ-Wide Gene Expression
1007 and Cell Atlas of the Developing Human Heart. *Cell,* 179**,** 1647-1660 e19.
1008 Bagley, J. A., Reumann, D., Bian, S., Levi-Strauss, J. andKnoblich, J. A. 2017. Fused cerebral
1009 organoids model interactions between brain regions. *Nat Methods,* 14**,** 743-751.
1010 Bao, X., Lian, X., Hacker, T. A., Schmuck, E. G., Qian, T., Bhute, V. J., Han, T., Shi, M.,
1011 Drowley, L., Plowright, A.*, et al.* 2016. Long-term self-renewing human epicardial cells
1012 generated from pluripotent stem cells under defined xeno-free conditions. *Nat Biomed*
1013 *Eng,* 1.
1014 Brown, B. N. andBadylak, S. F. 2014. Extracellular matrix as an inductive scaffold for functional
1015 tissue reconstruction. *Transl Res,* 163**,** 268-85.
1016 Brown, K., Doss, M. X., Legros, S., Artus, J., Hadjantonakis, A. K. andFoley, A. C. 2010.
1017 eXtraembryonic ENdoderm (XEN) stem cells produce factors that activate heart
1018 formation. *PLoS One,* 5**,** e13446.
1019 Cao, N., Liu, Z. M., Chen, Z. Y., Wang, J., Chen, T. T., Zhao, X. Y., Ma, Y., Qin, L. J., Kang, J.
1020 H., Wei, B.*, et al.* 2012. Ascorbic acid enhances the cardiac differentiation of induced
1021 pluripotent stem cells through promoting the proliferation of cardiac progenitor cells. *Cell*
1022 *Research,* 22**,** 219-236.
1023 Chakravarti, S. 2002. Functions of lumican and fibromodulin: lessons from knockout mice.
1024 *Glycoconj J,* 19**,** 287-93.
1025 Chan, S. S., Li, H. J., Hsueh, Y. C., Lee, D. S., Chen, J. H., Hwang, S. M., Chen, C. Y., Shih, E.
1026 andHsieh, P. C. 2010. Fibroblast growth factor-10 promotes cardiomyocyte
1027 differentiation from embryonic and induced pluripotent stem cells. *PLoS One,* 5**,** e14414.
1028 Chetaille, P., Preuss, C., Burkhard, S., Cote, J. M., Houde, C., Castilloux, J., Piche, J., Gosset,
1029 N., Leclerc, S., Wunnemann, F.*, et al.* 2014. Mutations in SGOL1 cause a novel
1030 cohesinopathy affecting heart and gut rhythm. *Nat Genet,* 46**,** 1245-9.
1031 Churko, J. M., Garg, P., Treutlein, B., Venkatasubramanian, M., Wu, H., Lee, J., Wessells, Q.
1032 N., Chen, S. Y., Chen, W. Y., Chetal, K.*, et al.* 2018. Defining human cardiac
1033 transcription factor hierarchies using integrated single-cell heterogeneity analysis. *Nat*
1034 *Commun,* 9**,** 4906.
1035 Cui, Y., Zheng, Y., Liu, X., Yan, L., Fan, X., Yong, J., Hu, Y., Dong, J., Li, Q., Wu, X.*, et al.*
1036 2019. Single-Cell Transcriptome Analysis Maps the Developmental Track of the Human
1037 Heart. *Cell Rep,* 26**,** 1934-1950 e5.
1038 Devine, W. P., Wythe, J. D., George, M., Koshiba-Takeuchi, K. andBruneau, B. G. 2014. Early
1039 patterning and specification of cardiac progenitors in gastrulating mesoderm. *Elife,* 3.
1040 Dignass, A. U. andSturm, A. 2001. Peptide growth factors in the intestine. *Eur J Gastroenterol*
1041 *Hepatol,* 13**,** 763-70.

1042 Drakhlis, L., Biswanath, S., Farr, C.-M., Lupanow, V., Teske, J., Ritzenhoff, K., Franke, A.,
1043 Manstein, F., Bolesani, E., Kempf, H., *et al.* 2021. Human heart-forming organoids
1044 recapitulate early heart and foregut development. *Nature Biotechnology*.
1045 El-Hariry, I., Pignatelli, M. andLemoine, N. 1997. Fibroblast growth factor 1 and fibroblast
1046 growth factor 2 immunoreactivity in gastrointestinal tumours. *J Pathol,* 181**,** 39-45.
1047 Engels, M. C., Rajarajan, K., Feistritzer, R., Sharma, A., Nielsen, U. B., Schalij, M. J., De Vries,
1048 A. a. F., Pijnappels, D. A. andWu, S. M. 2013. IGF promotes cardiac lineage induction
1049 by selective expansion of cardiogenic mesoderm in vitro. *European Heart Journal,* 34.
1050 Faustino Martins, J. M., Fischer, C., Urzi, A., Vidal, R., Kunz, S., Ruffault, P. L., Kabuss, L.,
1051 Hube, I., Gazzerro, E., Birchmeier, C., *et al.* 2020. Self-Organizing 3D Human Trunk
1052 Neuromuscular Organoids. *Cell Stem Cell,* 26**,** 172-186 e6.
1053 Feng, J., Meyer, C. A., Wang, Q., Liu, J. S., Shirley Liu, X. andZhang, Y. 2012. GFOLD: a
1054 generalized fold change for ranking differentially expressed genes from RNA-seq data.
1055 *Bioinformatics,* 28**,** 2782-8.
1056 Ferdous, Z., Wei, V. M., Iozzo, R., Hook, M. andGrande-Allen, K. J. 2007. Decorin-
1057 transforming growth factor- interaction regulates matrix organization and mechanical
1058 characteristics of three-dimensional collagen matrices. *J Biol Chem,* 282**,** 35887-98.
1059 Gays, D., Hess, C., Camporeale, A., Ala, U., Provero, P., Mosimann, C. andSantoro, M. M.
1060 2017. An exclusive cellular and molecular network governs intestinal smooth muscle cell
1061 differentiation in vertebrates. *Development,* 144**,** 464-478.
1062 Gribble, F. M. andReimann, F. 2016. Enteroendocrine Cells: Chemosensors in the Intestinal
1063 Epithelium. *Annu Rev Physiol,* 78**,** 277-99.
1064 Hill, M. A. 2020a. *Embryology Cardiovascular System - Heart Development* [Online]. UNSW
1065 Embryology. Available:
1066 https://embryology.med.unsw.edu.au/embryology/index.php/Cardiovascular_System_-
1067 _Heart_Development [Accessed 2020].
1068 Hill, M. A. 2020b. *Embryology Gastrointestinal Tract Development* [Online]. UNSW
1069 Embryology. Available:
1070 https://embryology.med.unsw.edu.au/embryology/index.php/Gastrointestinal_Tract_Dev
1071 elopment#:~:text=The%20gastrointestinal%20tract%20(GIT)%20arises,all%20the%20ge
1072 rm%20cell%20layers. [Accessed 2020].
1073 Hirakow, R. 1983. Development of the cardiac blood vessels in staged human embryos. *Acta*
1074 *Anat (Basel),* 115**,** 220-30.
1075 Holtzinger, A., Rosenfeld, G. E. andEvans, T. 2010. Gata4 directs development of cardiac-
1076 inducing endoderm from ES cells. *Dev Biol,* 337**,** 63-73.
1077 Hookway, T. A., Butts, J. C., Lee, E., Tang, H. andMcdevitt, T. C. 2016. Aggregate formation
1078 and suspension culture of human pluripotent stem cells and differentiated progeny.
1079 *Methods,* 101**,** 11-20.
1080 Hookway, T. A., Matthys, O. B., Mendoza-Camacho, F. N., Rains, S., Sepulveda, J. E., Joy, D.
1081 A. andMcdevitt, T. C. 2019. Phenotypic Variation Between Stromal Cells Differentially
1082 Impacts Engineered Cardiac Tissue Function. *Tissue Eng Part A,* 25**,** 773-785.
1083 Hosseini, H. S., Garcia, K. E. andTaber, L. A. 2017. A new hypothesis for foregut and heart tube
1084 formation based on differential growth and actomyosin contraction. *Development,* 144**,**
1085 2381-2391.
1086 Huebsch, N., Loskill, P., Mandegar, M. A., Marks, N. C., Sheehan, A. S., Ma, Z., Mathur, A.,
1087 Nguyen, T. N., Yoo, J. C., Judge, L. M., *et al.* 2015. Automated Video-Based Analysis of

1088 Contractility and Calcium Flux in Human-Induced Pluripotent Stem Cell-Derived
1089 Cardiomyocytes Cultured over Different Spatial Scales. *Tissue Engineering Part C-*
1090 *Methods,* 21**,** 467-479.
1091 Ishii, Y., Langberg, J. D., Hurtado, R., Lee, S. andMikawa, T. 2007. Induction of proepicardial
1092 marker gene expression by the liver bud. *Development,* 134**,** 3627-37.
1093 Judge, L. M., Perez-Bermejo, J. A., Truong, A., Ribeiro, A. J., Yoo, J. C., Jensen, C. L.,
1094 Mandegar, M. A., Huebsch, N., Kaake, R. M., So, P. L.*, et al.* 2017. A BAG3 chaperone
1095 complex maintains cardiomyocyte function during proteotoxic stress. *JCI Insight,* 2.
1096 Jung, J., Zheng, M., Goldfarb, M. andZaret, K. S. 1999. Initiation of mammalian liver
1097 development from endoderm by fibroblast growth factors. *Science,* 284**,** 1998-2003.
1098 Kelly, R. G., Brown, N. A. andBuckingham, M. E. 2001. The arterial pole of the mouse heart
1099 forms from Fgf10-expressing cells in pharyngeal mesoderm. *Dev Cell,* 1**,** 435-40.
1100 Kidokoro, H., Yonei-Tamura, S., Tamura, K., Schoenwolf, G. C. andSaijoh, Y. 2018. The heart
1101 tube forms and elongates through dynamic cell rearrangement coordinated with foregut
1102 extension. *Development,* 145**,** dev152488.
1103 Kim, D., Paggi, J. M., Park, C., Bennett, C. andSalzberg, S. L. 2019. Graph-based genome
1104 alignment and genotyping with HISAT2 and HISAT-genotype. *Nat Biotechnol,* 37**,** 907-
1105 915.
1106 Kim, H. D., Kim, D. J., Lee, I. J., Rah, B. J., Sawa, Y. andSchaper, J. 1992. Human fetal heart
1107 development after mid-term: morphometry and ultrastructural study. *J Mol Cell Cardiol,*
1108 24**,** 949-65.
1109 Kim, K. H., Nakaoka, Y., Augustin, H. G. andKoh, G. Y. 2018. Myocardial Angiopoietin-1
1110 Controls Atrial Chamber Morphogenesis by Spatiotemporal Degradation of Cardiac Jelly.
1111 *Cell Rep,* 23**,** 2455-2466.
1112 Kobayashi, M., Khalil, H. A., Lei, N. Y., Wang, Q., Wang, K., Wu, B. M. andDunn, J. C. Y.
1113 2018. Bioengineering functional smooth muscle with spontaneous rhythmic contraction
1114 in vitro. *Sci Rep,* 8**,** 13544.
1115 Koike, H., Iwasawa, K., Ouchi, R., Maezawa, M., Giesbrecht, K., Saiki, N., Ferguson, A.,
1116 Kimura, M., Thompson, W. L., Wells, J. M.*, et al.* 2019. Modelling human hepato-
1117 biliary-pancreatic organogenesis from the foregut-midgut boundary. *Nature,* 574**,** 112-
1118 116.
1119 Lancaster, M. A. andKnoblich, J. A. 2014. Organogenesis in a dish: Modeling development and
1120 disease using organoid technologies. *Science,* 345.
1121 Lee, J., Sutani, A., Kaneko, R., Takeuchi, J., Sasano, T., Kohda, T., Ihara, K., Takahashi, K.,
1122 Yamazoe, M., Morio, T.*, et al.* 2020. In vitro generation of functional murine heart
1123 organoids via FGF4 and extracellular matrix. *Nat Commun,* 11**,** 4283.
1124 Lee, J. H., Protze, S. I., Laksman, Z., Backx, P. H. andKeller, G. M. 2017. Human Pluripotent
1125 Stem Cell-Derived Atrial and Ventricular Cardiomyocytes Develop from Distinct
1126 Mesoderm Populations. *Cell Stem Cell,* 21**,** 179-194 e4.
1127 Lian, X., Hsiao, C., Wilson, G., Zhu, K., Hazeltine, L. B., Azarin, S. M., Raval, K. K., Zhang, J.,
1128 Kamp, T. J. andPalecek, S. P. 2012. Robust cardiomyocyte differentiation from human
1129 pluripotent stem cells via temporal modulation of canonical Wnt signaling. *Proc Natl*
1130 *Acad Sci U S A,* 109**,** E1848-57.
1131 Lian, X., Zhang, J., Azarin, S. M., Zhu, K., Hazeltine, L. B., Bao, X., Hsiao, C., Kamp, T. J.
1132 andPalecek, S. P. 2013. Directed cardiomyocyte differentiation from human pluripotent

1133 stem cells by modulating Wnt/beta-catenin signaling under fully defined conditions. *Nat*
1134 *Protoc,* 8**,** 162-75.
1135 Liao, Y., Smyth, G. K. andShi, W. 2014. featureCounts: an efficient general purpose program for
1136 assigning sequence reads to genomic features. *Bioinformatics,* 30**,** 923-30.
1137 Libby, A. R., Joy, D. A., So, P. L., Mandegar, M. A., Muncie, J. M., Mendoza-Camacho, F. N.,
1138 Weaver, V. M., Conklin, B. R. andMcdevitt, T. C. 2018. Spatiotemporal mosaic self-
1139 patterning of pluripotent stem cells using CRISPR interference. *Elife,* 7.
1140 Libby, A. R. G., Briers, D., Haghighi, I., Joy, D. A., Conklin, B. R., Belta, C. andMcdevitt, T. C.
1141 2019. Automated Design of Pluripotent Stem Cell Self-Organization. *Cell Syst,* 9**,** 483-
1142 495 e10.
1143 Lough, J. andSugi, Y. 2000. Endoderm and heart development. *Dev Dyn,* 217**,** 327-42.
1144 Lundy, S. D., Zhu, W. Z., Regnier, M. andLaflamme, M. A. 2013. Structural and functional
1145 maturation of cardiomyocytes derived from human pluripotent stem cells. *Stem Cells*
1146 *Dev,* 22**,** 1991-2002.
1147 Ma, J., Guo, L., Fiene, S. J., Anson, B. D., Thomson, J. A., Kamp, T. J., Kolaja, K. L., Swanson,
1148 B. J. andJanuary, C. T. 2011. High purity human-induced pluripotent stem cell-derived
1149 cardiomyocytes: electrophysiological properties of action potentials and ionic currents.
1150 *Am J Physiol Heart Circ Physiol,* 301**,** H2006-17.
1151 Ma, Z., Wang, J., Loskill, P., Huebsch, N., Koo, S., Svedlund, F. L., Marks, N. C., Hua, E. W.,
1152 Grigoropoulos, C. P., Conklin, B. R.*, et al.* 2015. Self-organizing human cardiac
1153 microchambers mediated by geometric confinement. *Nat Commun,* 6**,** 7413.
1154 Mackay, J. L., Sood, A. andKumar, S. 2014. Three-dimensional patterning of multiple cell
1155 populations through orthogonal genetic control of cell motility. *Soft matter,* 10**,** 2372-
1156 2380.
1157 Macqueen, L. A., Sheehy, S. P., Chantre, C. O., Zimmerman, J. F., Pasqualini, F. S., Liu, X.,
1158 Goss, J. A., Campbell, P. H., Gonzalez, G. M., Park, S. J.*, et al.* 2018. A tissue-
1159 engineered scale model of the heart ventricle. *Nat Biomed Eng,* 2**,** 930-941.
1160 Mandegar, M. A., Huebsch, N., Frolov, E. B., Shin, E., Truong, A., Olvera, M. P., Chan, A. H.,
1161 Miyaoka, Y., Holmes, K., Spencer, C. I.*, et al.* 2016. CRISPR Interference Efficiently
1162 Induces Specific and Reversible Gene Silencing in Human iPSCs. *Cell Stem Cell,* 18**,**
1163 541-53.
1164 Matthys, O. B., Silva, A. C. andMcdevitt, T. C. 2020. Engineering human organoid development
1165 ex vivo—challenges and opportunities. *Current Opinion in Biomedical Engineering,* 13**,**
1166 160-167.
1167 Mills, R. J., Titmarsh, D. M., Koenig, X., Parker, B. L., Ryall, J. G., Quaife-Ryan, G. A., Voges,
1168 H. K., Hodson, M. P., Ferguson, C., Drowley, L.*, et al.* 2017. Functional screening in
1169 human cardiac organoids reveals a metabolic mechanism for cardiomyocyte cell cycle
1170 arrest. *Proc Natl Acad Sci U S A,* 114**,** E8372-E8381.
1171 Mummery, C., Ward-Van Oostwaard, D., Doevendans, P., Spijker, R., Van Den Brink, S.,
1172 Hassink, R., Van Der Heyden, M., Opthof, T., Pera, M., De La Riviere, A. B.*, et al.* 2003.
1173 Differentiation of human embryonic stem cells to cardiomyocytes: role of coculture with
1174 visceral endoderm-like cells. *Circulation,* 107**,** 2733-40.
1175 Munera, J. O., Sundaram, N., Rankin, S. A., Hill, D., Watson, C., Mahe, M., Vallance, J. E.,
1176 Shroyer, N. F., Sinagoga, K. L., Zarzoso-Lacoste, A.*, et al.* 2017. Differentiation of
1177 Human Pluripotent Stem Cells into Colonic Organoids via Transient Activation of BMP
1178 Signaling. *Cell Stem Cell,* 21**,** 51-+.

1179 Nguyen, D. C., Hookway, T. A., Wu, Q., Jha, R., Preininger, M. K., Chen, X., Easley, C. A.,
1180 Spearman, P., Deshpande, S. R., Maher, K.*, et al.* 2014. Microscale generation of
1181 cardiospheres promotes robust enrichment of cardiomyocytes derived from human
1182 pluripotent stem cells. *Stem Cell Reports,* 3**,** 260-8.
1183 Perez-Pomares, J. M. andDe La Pompa, J. L. 2011. Signaling during epicardium and coronary
1184 vessel development. *Circ Res,* 109**,** 1429-42.
1185 Racca, A. W., Klaiman, J. M., Pioner, J. M., Cheng, Y., Beck, A. E., Moussavi-Harami, F.,
1186 Bamshad, M. J. andRegnier, M. 2016. Contractile properties of developing human fetal
1187 cardiac muscle. *J Physiol,* 594**,** 437-52.
1188 Rochais, F., Sturny, R., Chao, C. M., Mesbah, K., Bennett, M., Mohun, T. J., Bellusci, S.
1189 andKelly, R. G. 2014. FGF10 promotes regional foetal cardiomyocyte proliferation and
1190 adult cardiomyocyte cell-cycle re-entry. *Cardiovasc Res,* 104**,** 432-42.
1191 Ronaldson-Bouchard, K., Ma, S. P., Yeager, K., Chen, T., Song, L., Sirabella, D., Morikawa, K.,
1192 Teles, D., Yazawa, M. andVunjak-Novakovic, G. 2018. Advanced maturation of human
1193 cardiac tissue grown from pluripotent stem cells. *Nature*.
1194 Rossi, G., Broguiere, N., Miyamoto, M., Boni, A., Guiet, R., Girgin, M., Kelly, R. G., Kwon, C.
1195 andLutolf, M. P. 2020. Capturing Cardiogenesis in Gastruloids. *Cell Stem Cell*.
1196 Rudy-Reil, D. andLough, J. 2004. Avian precardiac endoderm/mesoderm induces cardiac
1197 myocyte differentiation in murine embryonic stem cells. *Circ Res,* 94**,** e107-16.
1198 Rutenberg, J. B., Fischer, A., Jia, H., Gessler, M., Zhong, T. P. andMercola, M. 2006.
1199 Developmental patterning of the cardiac atrioventricular canal by Notch and Hairy-
1200 related transcription factors. *Development,* 133**,** 4381-90.
1201 Sato, T., Vries, R. G., Snippert, H. J., Van De Wetering, M., Barker, N., Stange, D. E., Van Es, J.
1202 H., Abo, A., Kujala, P., Peters, P. J.*, et al.* 2009. Single Lgr5 stem cells build crypt-villus
1203 structures in vitro without a mesenchymal niche. *Nature,* 459**,** 262-265.
1204 Schultheiss, T. M., Xydas, S. andLassar, A. B. 1995. Induction of avian cardiac myogenesis by
1205 anterior endoderm. *Development,* 121**,** 4203-14.
1206 Sergeeva, I. A. andChristoffels, V. M. 2013. Regulation of expression of atrial and brain
1207 natriuretic peptide, biomarkers for heart development and disease. *Biochim Biophys Acta,*
1208 1832**,** 2403-13.
1209 Shen, H., Cavallero, S., Estrada, K. D., Sandovici, I., Kumar, S. R., Makita, T., Lien, C. L.,
1210 Constancia, M. andSucov, H. M. 2015. Extracardiac control of embryonic cardiomyocyte
1211 proliferation and ventricular wall expansion. *Cardiovasc Res,* 105**,** 271-8.
1212 Smits, A. M., Dronkers, E. andGoumans, M. J. 2018. The epicardium as a source of multipotent
1213 adult cardiac progenitor cells: Their origin, role and fate. *Pharmacol Res,* 127**,** 129-140.
1214 Stennard, F. A. andHarvey, R. P. 2005. T-box transcription factors and their roles in regulatory
1215 hierarchies in the developing heart. *Development,* 132**,** 4897-4910.
1216 Sugi, Y. andLough, J. 1994. Anterior Endoderm Is a Specific Effector of Terminal Cardiac
1217 Myocyte Differentiation of Cells from the Embryonic Heart Forming Region.
1218 *Developmental Dynamics,* 200**,** 155-162.
1219 Sugi, Y. andLough, J. 1995. Activin-A and FGF-2 mimic the inductive effects of anterior
1220 endoderm on terminal cardiac myogenesis in vitro. *Dev Biol,* 168**,** 567-74.
1221 Takasato, M., Er, P. X., Chiu, H. S., Maier, B., Baillie, G. J., Ferguson, C., Parton, R. G.,
1222 Wolvetang, E. J., Roost, M. S., Lopes, S. M.*, et al.* 2016. Kidney organoids from human
1223 iPS cells contain multiple lineages and model human nephrogenesis. *Nature,* 536**,** 238.

1224 Turaga, D., Matthys, O. B., Hookway, T. A., Joy, D. A., Calvert, M. andMcdevitt, T. C. 2020.
1225 Single-Cell Determination of Cardiac Microtissue Structure and Function Using Light
1226 Sheet Microscopy. *Tissue Eng Part C Methods,* 26**,** 207-215.
1227 Uosaki, H., Andersen, P., Shenje, L. T., Fernandez, L., Christiansen, S. L. andKwon, C. 2012.
1228 Direct contact with endoderm-like cells efficiently induces cardiac progenitors from
1229 mouse and human pluripotent stem cells. *PLoS One,* 7**,** e46413.
1230 Varner, V. D. andTaber, L. A. 2012. Not just inductive: a crucial mechanical role for the
1231 endoderm during heart tube assembly. *Development,* 139**,** 1680-1690.
1232 Volpato, V. andWebber, C. 2020. Addressing variability in iPSC-derived models of human
1233 disease: guidelines to promote reproducibility. *Dis Model Mech,* 13.
1234 Wheelwright, M., Win, Z., Mikkila, J. L., Amen, K. Y., Alford, P. W. andMetzger, J. M. 2018.
1235 Investigation of human iPSC-derived cardiac myocyte functional maturation by single
1236 cell traction force microscopy. *PLoS One,* 13**,** e0194909.
1237 Xiang, Y., Tanaka, Y., Patterson, B., Kang, Y. J., Govindaiah, G., Roselaar, N., Cakir, B., Kim,
1238 K. Y., Lombroso, A. P., Hwang, S. M.*, et al.* 2017. Fusion of Regionally Specified hPSC-
1239 Derived Organoids Models Human Brain Development and Interneuron Migration. *Cell*
1240 *Stem Cell,* 21**,** 383-398 e7.
1241 Yang, H., Borg, T. K., Wang, Z., Ma, Z. andGao, B. Z. 2014. Role of the Basement Membrane
1242 in Regulation of Cardiac Electrical Properties. *Annals of biomedical engineering,* 42**,**
1243 1148-1157.
1244 Zhang, H. T. andHiiragi, T. 2018. Symmetry Breaking in the Mammalian Embryo. *Annu Rev*
1245 *Cell Dev Biol,* 34**,** 405-426.
1246 Zhang, Z., Yu, D., Seo, M., Hersh, C. P., Weiss, S. T. andQiu, W. 2019. Novel Data
1247 Transformations for RNA-seq Differential Expression Analysis. *Sci Rep,* 9**,** 4820.
1248